Dual-acting gene therapy targeting HIF1A and HIF2A by RNA interference mitigates retinal degeneration in two mouse models of AMD

Lynn J. A. Ebner[1,2], Cornelia Imsand[1], Duygu Karademir[1,3], Florian Peters[1,4], Eva Kiessling[1,5], Antonia Fottner[1], Claudia Matter[1], Diego S. Fajardo[6], Luca Merolla[1], Gabriele M. Wögenstein[1], Ioanna Tsioti[1], Larissa P. Govers[1], Frank Blaser[7], Isabelle Meneau[7], Sanford L. Boye[6], Shannon E. Boye[8], Christian Grimm[1,+], Marijana Samardzija[1,*,+]

[1] Laboratory for Retinal Cell Biology, Department of Ophthalmology, University Hospital Zurich, University of Zurich, Wagistrasse 14, Schlieren, 8952, Zurich, Switzerland.

[2] Present address: Roche Pharma Research and Early Development, Roche Innovative Center, F. Hoffmann-La Roche Ltd, Grenzacherstrasse 124, Basel, 4070, Basel-Stadt, Switzerland (lynn.ebner@roche.com)

[3] Present address: Institute of Molecular and Clinical Ophthalmology Basel, Switzerland

[4] Present address: Department of Clinical Research, University of Basel, University Hospital Basel, Basel, Switzerland

[5] Present address: Lonza AG, Rottenstrasse 6, 3930 Visp, Switzerland

[6] Department of Pediatrics, Powell Gene Therapy Center, University of Florida; Gainesville, FL, USA.

[7] Department of Ophthalmology, University Hospital Zurich, Switzerland

[8] Department of Pediatrics, Division of Cellular and Molecular Therapy, University of Florida, Gainesville, Florida, USA

[+] Equal contributions

[*] Corresponding author

lynn.ebner@roche.com
dallo.imsand@bluewin.ch
duygu.sigurdsson@iob.ch
florian.peters@usb.ch
eva.kiessling@lonza.com
antonia.fottner@usz.ch
Claudia.matter@usz.ch
diegof@ufl.edu
luca.merolla@uzh.ch
gabriele.woegenstein@uzh.ch
ioanna.tsioti@uzh.ch
larissa.govers@uzh.ch
frank.blaser@usz.ch
isabelle.meneau@usz.ch
sboye@ufl.edu
shaire@ufl.edu
cgrimm@opht.uzh.ch
marijana.samardzija@usz.uzh.ch

Abstract

Background: The combination of reduced choroidal blood flow, increased Bruch´s membrane (BM) thickness and drusen formation leads to reduced oxygenation of the outer retina in the aging eye and contributes to the pathology of age-related macular degeneration (AMD). This implies that the molecular response of photoreceptors to hypoxia, with chronic activation of hypoxia-inducible factors (HIFs) at its core, impacts disease development and progression.

Methods: We used the shRNAmiR system to develop a dual-acting gene therapy based on a single AAV that reduces activity of HIF1 in photoreceptors and HIF2 in the retinal pigment epithelium (RPE). The virus was injected subretinally in two models of pseudo ($Rod^{\Delta Vhl}$) or true ($RPE^{\Delta Vegfa}$) hypoxia-related retinal degeneration and treated mice were followed for up to 61 weeks post-injection. Light microscopy, fluorescence funduscopy, and optical coherence tomography were used to quantify the therapeutic effect. *In situ* hybridization, real-time PCR, Western blotting, immunofluorescence, and flatmounts of the retina, RPE, and choroid were used to investigate the disease models and therapeutic effects of the treatment.

Results: No adverse effects were noted after subretinal injection of the AAV expressing shRNAs targeting *Hif1a* in photoreceptors and *Hif2a* in the RPE. The virus preserved ONL thickness and photoreceptor segment length in $Rod^{\Delta Vhl}$ mouse retinas up to 22 weeks and in $RPE^{\Delta Vegfa}$ mice up to 61 weeks after injection demonstrating a long-lasting rescue of the phenotype. The dual-acting virus showed significantly higher efficacy than single-acting viruses targeting solely *Hif1a* in photoreceptors or *Hif2a* in the RPE.

Conclusion: This study introduces a novel dual-acting AAV vector that effectively downregulates two different genes in two specific cell types, offering a promising therapeutic strategy for complex diseases such as AMD. By simultaneously targeting *Hif1a* in photoreceptors and *Hif2a* in the retinal pigment epithelium, this gene-agnostic therapy shows

significant potential to protect retinal tissues from chronic hypoxic conditions. By targeting a common and conserved disease pathway in AMD, it is applicable to a wide range of patients.

Keywords:

Hypoxia; HIF1; HIF2; retinal degeneration; age related macular degeneration; photoreceptor; retinal pigment epithelium; gene therapy; RNA interference; AAV

Background

Undisturbed retinal and choroidal blood flow is essential to satisfy the metabolic needs of retinal cells with their high demand for oxygen and nutrients. With advancing age, however, various tissue changes may affect choroidal vasculature and decrease oxygen supply to the retina. These changes include reduced choroidal thickness and blood flow, decreased choroidal blood volume, endothelial cell loss leading to ghost vessel formation and reduced vessel density in the choriocapillaris, thickening of Bruch's membrane and accumulation of drusen deposits (1–4). As a consequence, tissue hypoxia may evolve leading to increased expression of hypoxia-inducible genes including vascular endothelial growth factor A (*VEGFA*) in the retina of older donors (5). Reduced tissue oxygenation and increased VEGFA secretion are established drivers for neovascularization in exudative (wet) age-related macular degeneration (AMD) and vascular pathologies in other retinal diseases, including diabetic retinopathy. Notably, these age-dependent tissue changes may also be of significance for the non-exudative (dry) form of AMD as they were correlated to drusen formation (1–4) and suggested to precede degeneration of photoreceptors or the retinal pigment epithelium (RPE) (6).

The primary defects in AMD are suggested to lie within the Bruch's membrane (7, 8) and the RPE (9–11). As AMD progresses, the consecutive degeneration of photoreceptors in the macular area leads to reduced visual acuity and substantial vision loss. To prevent disease progression and to broaden the treatment window, an effective therapy should thus target

both primary and secondary disease events and ideally act on the RPE as well as photoreceptors. Therefore, modulating the cellular response to hypoxia emerges as a promising treatment approach, especially since the molecules responsible for hypoxia-related RPE and photoreceptor degeneration have already been identified in animal models. While overactivation of hypoxia-inducible factor 2 (HIF2) but not HIF1 in the RPE causes RPE atrophy and retinal thinning (10), constitutively active HIF1 but not HIF2 in photoreceptor cells induces photoreceptor degeneration (5, 12). Cell loss and degeneration can thus be prevented by the genetic inactivation of *Hif2a* in the RPE (10) and *Hif1a* in photoreceptors. This indicates that a successful therapy needs to specifically reduce the expression of the respective *Hifa* isoform in the two distinct cell types.

Conventional therapeutic RNA knockdown strategies using small interfering RNAs (siRNAs) are often limited because they interfere with endogenous microRNA biogenesis, lead to an overload of transport proteins, or cause other unwanted side effects (13–15). To circumvent such problems, we generated a multiplex RNAi approach using the microRNA-based shRNAmiR system that directs the therapeutic RNAs into the miRNA pathway already at the level of DROSHA in the cell nucleus (16, 17). Sequential processing by DROSHA and DICER ensures the generation of precisely cleaved siRNAs while minimally affecting the natural microRNA processing machinery (17). This increases efficiency while reducing off-target effects and minimizes immune responses (18, 19). The use of the miR-E instead of the conventional miR-30 backbone for shRNA expression increases the knockdown efficiency of target genes and allows cell-type specific expression when placed in the 3'UTR of genes that are controlled by Pol-II promoters (20). Using this system, we developed a novel dual-acting gene therapy that simultaneously targets *Hif1a* in photoreceptors and *Hif2a* in the RPE. The therapeutic potential was validated and tested in two mouse models of hypoxia-related retinal degeneration and shown to significantly improve tissue integrity and photoreceptor survival in both animal models of AMD.

Methods

Animals

Animal experimentation was approved by the Cantonal Veterinary Office of Zürich, Switzerland (license numbers: ZH019/2019 and ZH105/2022) and adhered to the ARVO statement for the use of Animals in Ophthalmic and Vision Research. Wild type (B6/J-Crl1*)* and transgenic mice were maintained as breeding colonies at the Laboratory Animal Service Center (LASC) of the University Zürich with a 14/10 h light-dark cycle with an average light intensity of 60-150 lux at cage level. Mice had access to food and water *ad libitum*. *Vhl*$^{fl/fl}$ mice (21) were mated to *Vhl*$^{fl/fl}$ mice heterozygous for OpsinCre (LMOPC1, (22)) to generate *Vhl*$^{fl/fl}$*;OpsinCre* (*Rod*$^{\Delta Vhl}$) mice and *Vhl*$^{fl/fl}$ control littermates as described (Lange et al., 2011). *Vegfa*$^{fl/fl}$ animals were kindly provided by Christian Stockmann, Institute of Anatomy, University of Zürich (23). Individual eyes of mice of both sexes were randomly assigned to treatment or control.

Human tissue samples

Human donor eyes without cornea and lens were received from the eyebank of the University Hospital Zurich in ice-cold PBS. The use of the tissue for research was approved by the ethics committee of Zurich, Switzerland (BASEC-Nr: PB_2017-00550 and 2020-01856) and adhered to the tenets of the Declaration of Helsinki. The vitreous was carefully removed and four incisions were used to flatmount the tissue. Retina and RPE samples were collected from the nasal periphery and the central (macular) region (Fig. 1F). RNA was isolated from the samples using the RNeasy kit (Qiagen, Hilden, Germany). cDNA synthesis and real-time PCR were performed using human specific primer pairs (Table 1), following the same methods as described for the mouse samples (see below).

Cloning and generation of AAVs

shRNAmiR DNA fragments containing *shHif1a*, *shHif2a* or *shCtrl* sequences were designed using the miR-E backbone following the recommendation by Fellmann (20) (Fig. S1A-C) and produced by Bio-Synthesis (Bio-Synthesis Inc. TX, USA). The *shHif1a* and *shHif2a* RNAmiR fragments were cloned into the 3'UTRs of GFP and mCherry, respectively. To achieve cell-specificity, the G-protein-coupled kinase 1 (GRK1) promotor was used for expression of GFP (and thus *shHif1a*) in photoreceptors, and the vitelliform macular dystrophy 2 (VMD2, alias bestrophin 1) promoter for expression of mCherry (and thus *shHif2a*) in the RPE. This dual-acting viral construct is named shHif from here on (Fig. 2D). The shCtrl construct had a scrambled shRNA sequence cloned into the miR-E backbone in the 3'UTRs of both fluorescent genes (Fig. 2D). The complete plasmid sequences of plasmids *'shHif'* and *'shCtrl'* are given in supplemental data SD1. Plasmids for the single-acting AAVs contained either the GRK1-GFP-shHif1a or the VMD2-mCherry-shHif2a cassette (Fig. 2D). shHif*,* shHif1*,* shHif2 and shCtrl viruses were packed into an AAV8 with the three mutations Y447F, Y733F and T494V (AAV8-TM) (24). An AAV4::VMD2-Cre-P2A-GFP (25), was used to knockout *Vegfa* in the RPE of *Vegfa*$^{fl/fl}$ mice and an AAV4::VMD2-GFP served as control virus. Specifics of all AAVs are provided in Table 2. All AAVs have type 2 ITRs and were produced by the Viral Vector Facility of the University Zürich.

Subretinal injections

Injections were performed between post-natal days (PND) 27-30 as described by Gasparini et al (26). Briefly, pupils were dilated with 1% cyclogyl (Alcon Pharmaceuticals, Fribourg, Switzerland) and one drop of 5% neosynephrin (Ursapharm Schweiz GmbH, Hünenberg, Switzerland), and corneas were kept moist with viscotears (Bausch & Lomb Swiss AG, Zug, Switzerland). Mice were anesthetized with a subcutaneous injection of ketamin (85 mg/kg, Parke-Davis, Berlin, Germany) / xylazine (10 mg/kg, Bayer AG, Leverkusen, Germany) and placed on a heating pad set to 37°C during the procedure. The head was held by a stereotactic adapter (Hugo Sachs Elektronik – Harvard Apparatus GmbH, March-Hugstetten,

Germany) and the temporal sclera punctured with a 30G needle just beneath the ora serrata. A 5 µL Hamilton syringe (Hamilton Bonaduz AG, Bonaduz, Switzerland), placed in a micromanipulator (H. Saur Laborbedarf, Reutligen, Germany), was inserted gently through the pre-punctured site for transvitreal subretinal injections of 1 µL AAV solution approximately 15-25° nasally of the optic nerve. All AAVs were applied at a concentration of $5x10^8$ vg/µL, except for AAV4::VMD-Cre-P2A-eGFP ($1x10^9$ vg/µL) when used to generate *RPE*$^{\Delta Vegfa}$ mice for characterization (Fig. 4). To visualize and control injections, the injection solution was supplemented with 10% fluorescein (0.1 mg/mL, Akorn Inc., IL, USA). After injections, anesthesia was reversed with atipazemole (2 mg/kg, Graeub, Bern, Switzerland) and mice were placed on a heating pad until fully awake.

Funduscopy, optical coherence tomography, angiography, and volume scans

Anesthesia and pupil dilation were performed as described above. One drop of 2% methocel (OmniVision AG, Neuhausen, Switzerland) was applied to keep the eyes moist. Fundus images and optical coherence tomography (OCT) scans were acquired using the Micron IV system (Phoenix Research Labs, Pleasanton, CA, USA) as described (27). For fluorescein angiography mice were injected intraperitoneally with 30 µL of 2% fluorescein (Akorn Inc., IL, USA) and retinal vasculature was imaged with the Micron IV system. For *in vivo* quantification of retinal thickness, volume scans were performed using a Spectralis OCT-2 device (Heidelberg Engineering Inc., Heidelberg, Germany) with a 25-diopter lens. Animals were placed on a custom-built holder and kept warm with an integrated water heating system. An atraumatic focal contact lens was placed on the cornea moistened with a drop of viscotears (Bausch & Lomb) to improve imaging quality. The optic scan area was aligned to the optic nerve head and 25 consecutive high-resolution B-scans, each consisting of 1024 A-scans, were acquired. Automatic real-time tracking was set to 50. The built-in semi-automated segmentation tool (Spectralis software version 6.7.13.0, Eye Explorer software version 1.9.14.0) was utilized, and manual adjustments were done by blinded, experienced users (L.E., C.I., M.S.) to measure outer nuclear layer (ONL) thickness. To delineate fundus

areas, an Early Treatment Diabetic Retinopathy Study (ETDRS) circular grid with 9 subfields (1, 2.22, 3.45) was aligned to the optic nerve head (ON). ONL thickness was quantified in two (*RPE*$^{\Delta Vegfa}$ mice) or seven subfields (*Rod*$^{\Delta Vhl}$ mice). For *in vivo* quantification, the data were averaged per subfield (fundi with ETDRS grids, left) before calculating the average over all subfields and provided as data point for each eye (graphs, right).

Scotopic and photopic electroretinogram

Mice were dark-adapted overnight. Pupils were dilated and animals anesthetized as described above. Electroretinograms (ERG) were recorded simultaneously from both eyes using the Diagnosys Celeris rodent ERG device (Diagnosys, Cambridge, UK). Stimulus intensities ranging from $8x10^{-6}$ to 3 cd*s/m^2 were used for scotopic measurements. After a 5-min exposure to rod-suppressive background light (30 cd/m^2), photopic recordings were acquired using single-flash intensities ranging from 1 to 200 cd*s/m^2 with the background light on. For each stimulus intensity, five traces were averaged under scotopic and ten traces under photopic conditions.

RNA isolation and real-time PCR

Mice were euthanized with CO_2 inhalation followed by decapitation. Retinas were isolated through a slit in the cornea and snap-frozen in liquid nitrogen. In some instances, the remaining eyecup (EC) containing the RPE was cleaned from excessive tissue including the cornea and snap-frozen. RNA from tissues or cells was isolated using an RNA isolation kit (NucleoSpin RNA, Macherey-Nagel GmbH & co.KG, Düren, Germany) according to the manufacturer's instructions, including a DNase digestion step on the column. First-strand cDNA synthesis was performed by M-MLV reverse transcriptase (Promega, Dübendorf, Switzerland) using 1 µg total RNA and oligo-dT primers. Gene expression was analyzed via semi-quantitative real-time PCR (QuantStudio 3, Thermo Fisher Scientific, MA, USA) using 10 ng of cDNA template and PowerUp SYBR green Master Mix (Thermo Fisher Scientific). Primers pairs (Table 1) were designed to span large intronic regions and avoid known single

nucleotide polymorphisms in the mouse sequence. Normalization was performed with β-Actin (*Actb)* as housekeeping gene, and relative expression was calculated using the comparative threshold cycle method ($2^{-\Delta\Delta CT}$).

Morphology and immunofluorescence

Morphology and immunofluorescence analyses were performed as described (28). For morphology, dorsally marked eyes were enucleated from non-perfused ($Rod^{\Delta Vhl}$) or perfused ($RPE^{\Delta Vegfa}$; 4% paraformaldehyde (PFA)) mice and subsequently fixed in 2.5% glutaraldehyde at 4°C overnight. Eyes were postfixed in 1% osmium tetroxide and embedded in Epon812. Nasal-temporal sections (0.5 µm) were cut through the optic nerve head, counterstained with toluidine blue, and analyzed by light microscopy (AxioImager Z2, Carl Zeiss AG, Feldbach, Switzerland). ONL thickness and PS length were measured every 200 µm (from the optic nerve head) along reconstructed panorama images using Adobe Photoshop CS6 ruler tool (Adobe Systems, Inc.).

Eyes for immunofluorescence analysis were labelled dorsally and fixed in 4% PFA for 1 h. After removal of the lens and post-fixation for an additional hour, eyes were cryoprotected in 30% sucrose (Sigma-Aldrich, St. Louis, MO, USA) overnight, embedded and frozen in freezing medium (O.C.T., Leica Biosystems, Nussloch, Germany). Eyes were stored at -80°C until sectioned into 12 µm thin nasal-temporal sections. Immunolabelling was performed overnight at 4°C with primary antibodies (Table 3) in blocking solution containing 3% normal goat serum (Sigma-Aldrich) and 0.3% Triton X-100 (Sigma-Aldrich) in phosphate buffer. On the next day, sections were washed and incubated with the appropriate secondary antibodies in blocking solution for 1 h. Counterstaining was done with 4',6-diamidino-2-phenylindole (DAPI) before sections were mounted with MOWIOL (Sigma-Aldrich) antifade medium and imaged using a fluorescence microscope (AxioImager Z2, Carl Zeiss AG). Pixel intensity measurements were performed using ImageJ (Version 1.52a) by analyzing 250 µm long regions within transduced and non-transduced areas. The automatic threshold function was used to identify signal and background pixels. Pixels with an intensity of '0' were counted as

background/gaps. The cumulative length of these zero-intensity regions was calculated and presented as gap size per 250 µm.

In-situ hybridization

In-situ hybridization was performed with the RNAscope 2.5 HD RED Detection Kit (Cat. No. 322350, BioTechne/ACD, Minneapolis, USA). Cryosections were prepared as described above, baked at 60°C for 30 min, and post-fixed in 4% PFA for 15 min at 4°C. Slides were dehydrated for 5 min each in 50%, 70% and 100% ethanol and dried for 10 min at 60°C. Antigen retrieval was performed using hydrogen peroxide for 10 min, washed and followed by overnight incubation with target retrieval buffer (BioTechne/ACD). Protease Plus treatment was performed for 15 min at 40°C, followed by 2 x 30 s washings with H_2O, and incubation with the *Vegfa* probe (Cat. No. 521471, Mn-Vegfa-O3, BioTechne/ACD) for 2 h at 40°C. Probes were washed 2 x 5 min with wash buffer and incubated at 40°C with each amplifier (1-6) for 15-30 min, with two 5-minute washes conducted between each amplification step. The positive control probe *Mm-Polr2a* (Cat. No. 312471, BioTechne/ACD) and the negative control probe diluent (Cat. No. 300041, BioTechne/ACD) were used to validate experimental conditions. Slides were stained in 50% hematoxylin for 20 s, destained in H_2O, incubated in 0.02% ammonia water for 10 s, and washed again. Finally, slides were dried for 30 min at 60°C and mounted with Ecomount (Cat. No. 320409, BioTechne/ACD).

Retina- and RPE-flatmounts

After eyes were enucleated and incubated in 4% PFA for 10 min, corneas were opened and eyes incubated for another 20 min in PFA. The eyes were cut along the ora serrata to remove the cornea and placed on a nylon membrane (Boehringer Ingelheim, Ingelheim am Rhein, Germany). 5-6 radial incisions were made to flatten the eyecup and retina, and the lens was removed. Retina and eyecup were then separated and held flat between 2 membranes during an additional hour of fixation in 4% PFA. Flattened retinas or eyecups were removed from the membrane, washed with PBS, and blocked with 3% normal goat

serum (Sigma-Aldrich, St. Louis, MO, USA) and 0.3% Triton X-100 (Sigma-Aldrich) in PBS for 1-2 h. Incubation with primary antibodies (Table 3) was overnight at 4°C. Flatmounts were washed 3 x 10 min with PBS and incubated with the appropriate secondary antibodies for 1 h at room temperature. Subsequently, retinas and eyecups were washed 3 x 10 min with PBS, mounted, and imaged using a fluorescence microscope AxioImager Z2 (Carl Zeiss AG) or Leica DMI6000B (Leica Microsystems, Wetzlar, Germany).

Choroidal flatmounts

After an initial 30 min fixation in 4% PFA, eyes for choroidal flatmounts were washed in PBS and incubated at 55°C in pre-warmed 10% H_2O_2 for 2 to 2.5 h to bleach RPE and choroidal pigments. The cornea was removed by cutting along the ora serrata, and the eyes were placed on a nylon membrane. Lens and retina were removed, and four radial incisions were made to flatten the choroidal eyecup. The flattened tissue, secured between 2 nylon membranes, underwent an additional fixation step in 4% PFA for 1 h. Staining for podocalyxin-like (PODXL) proceeded as above, with the modifications that incubation with the primary antibody lasted for 2 days, and 3% horse serum (Sigma-Aldrich) was used for blocking.

Lentiviral-mediated gene silencing in 661W cells and hypoxic exposure

661W (29) and HEK293T cells (ATCC CRL-3216) cells were cultured in DMEM, 10% heat-inactivated FBS (Gibco, Thermo Fisher Scientific) and 1% penicillin-streptomycin (Gibco, Thermo Fisher Scientific) at 37°C and 5% CO_2. Lentiviral-pseudotyped particles were used to generate stable cell lines expressing shRNA against *Hif1a* (TRCN0000232222) or *Hif2a* (TRCN0000082303, TRCN0000082307, TRCN0000436203, TRCN0000416474, TRCN0000428636, TRCN0000082306) or a non-targeted scrambled shRNA (shCtrl, SHC002) (Sigma-Aldrich). To prepare lentiviral particles, HEK293T cells were seeded in 75 cm^2 culture flasks and co-transfected with shRNAs in combination with the ViraPower lentiviral expression vector system and Lipofectamin 3000 (Invitrogen, Thermo Fisher

Scientific) in serum-free medium. Medium was replaced the next day with medium containing FBS. The culture supernatants containing the lentivirus particles were collected 48-72 h post-transfection, cleared by centrifugation at 200 g for 5 min, and filtered through a 0.45 µm pore size filter (Merck & Cie, Schaffhausen, Switzerland). Filtrates were applied in a 1:1 mixture with medium containing 6 µg/mL polybrene (Sigma-Aldrich) to infect 661W cells. Infected cells were selected with 2 µg/mL puromycin for 2 weeks. Stable cell lines expressing *shHif1a*, *shHif2a,* and *shCtrl* were seeded at a density of 30,000 cells/mL in a 6-well plate and incubated overnight. Prior to hypoxic exposure, medium was exchanged, and cells were exposed to normoxia (21% O_2) or hypoxia (0.2% O_2 for 24 h). Subsequently, cells were harvested and prepared for Western blotting (see below) or real-time PCR (see above).

Western blotting

Cells were washed with PBS and 50 µL lysis buffer (1 M Tris, 150 mM NaCl, 1 mM Na_3VO_4, 1% Triton X-100, protease inhibitor (1 tablet per 10 ml solution; cOmplete ULTRA Tablets-Mini, F. Hoffmann-La Roche AG, Basel, Switzerland) was added. Cells were scraped off the plate, homogenized by sonication for 10 min and centrifuged (3 min 1000 rcf) at room temperature. The protein concentration was determined in the supernatant with a BCA protein assay kit (Pierce™, Thermo Scientific) according to manufacturer's instructions. DNA present in the homogenate was digested at 37°C for 1 h with 125 units benzonase (Sigma-Aldrich, St. Louis, MO, USA) before 70 µg of proteins were used for standard Western blotting. Primary antibodies (Table 3) were diluted in 5% non-fat blocking milk (BioRad, Cressier, Switzerland) in TBST and incubated over night at 4°C with mild agitation. HRP-conjugated secondary antibodies were used for signal detection by the Western lightning chemiluminescence reagent (PerkinElmer, Waltham, MA, USA) and exposure to X-ray films.

Statistical analysis

Statistical analysis was performed using GraphPad Prism (GraphPad Software, San Diego, CA, USA). Significance was tested by an unpaired t-test when two independent groups were

compared. When more than 2 groups were compared, a one-way ANOVA followed by a Tukey's (when all groups were compared to each other) or Dunnett's (when all groups were compared to a specific group) multiple comparison test was applied. Data were considered to be statistically different with $p \leq 0.05$. P-values are given directly in figures or in Table S1. All tests and number of animals/samples are indicated in the figure legends.

Results

Age-related expression of hypoxia-regulated genes in the human eye

We determined the expression of *VEGFA*, angiopoietin like 4 (*ANGPTL4*) and serpin family E member 1 (*SERPINE1*) in the central (macular) and peripheral (nasal) retina and RPE of human donor eyes. Expression in old eyes (71 – 94 y, median: 82 y) was compared to expression in young eyes (17 – 55 y, median: 35 y) without known ocular pathology and to age-matched AMD eyes (75 – 96 y, median: 88 y; Fig. 1A-C). All three genes are associated with AMD (30–32) and known to be regulated by hypoxia (31, 33, 34). Expression of complement factor H (*CFH)*, another AMD-associated gene (35) but not reported to be regulated by hypoxia, and G protein subunit alpha transducin 2 (*GNAT2*), a gene essential for phototransduction in cones (36), were included as controls (Fig.1D,E). All three hypoxia-regulated genes (*VEGFA*, *ANGPTL4* and *SERPINE1*) showed an age-dependent increase in expression in both the neuronal retina and the RPE. The increase was generally more pronounced in the peripheral regions of both the retina and the RPE. No differences were found when the central and the peripheral tissues of all normal donor eyes were compared, except for *SERPINE1* that was more strongly expressed in the central RPE (Fig 1, middle panels). *VEGFA* but not *ANGPTL4* or *SERPINE1* was differently expressed in normal and AMD eyes (Fig.1, right panels). Interestingly, expression of *VEGFA* was increased in the RPE but decreased in the retina of AMD donors. In contrast to these hypoxia-regulated genes, *CFH* was not differentially expressed in young and old retinas but had slightly higher

levels in the periphery of aged RPE of normal donors. No differences were found between the central and peripheral tissues. However, *CFH* expression was significantly reduced in the retina of AMD donors. The cone-specific *GNAT2* transcript exhibited reduced expression in both central and peripheral retinas of older donors as reported before (5), but was not differently expressed in AMD eyes (Fig. 1E). Our findings support the hypothesis that the retina and RPE of old eyes experience hypoxia, which upregulates genes known to be regulated at least in part by HIF transcription factors such as VEGFA, ANGPTL4, and SERPINE1 (31, 33, 34). Targeting HIF transcription factors in the retina and RPE of old eyes may thus normalize gene expression in these tissues and confer significant therapeutic benefits.

Efficient targeting of *Hif1a* and *Hif2a* using the shRNAmiR system

Chronically active HIF1 is the main driver for degeneration of photoreceptors, while HIF2 is the pathologic isoform in RPE cells (5, 10). Thus, to prevent hypoxia-related degeneration, we developed an RNA interference strategy that simultaneously represses HIF1 in photoreceptors and HIF2 in the RPE by targeting the mRNAs for the respective HIF alpha subunits in the specific cell types. To reduce *Hif1a* expression, we used a published and previously validated shHif1a RNA sequence that targets both the mouse and human sequence (5) and refer to this sequence as shHif1. To identify an efficient shHif2a sequence, six different shRNAs (shHif2_1-6) were stably expressed in 661W cells and tested for their efficiency to reduce expression of *Hif2a*. All six shRNAs were similarly efficient and reduced *Hif2a* mRNA levels in hypoxic cells (6 h, 0.2% O_2) to 2 - 9% when compared to the shCtrl sequence (Fig. S2). Since mouse shHif2_6 has only one mismatch to the human *HIF2A* RNA, all further experiments were performed using this sequence, which will be referred to as shHif2.

Hif1a and *Hif2a* mRNA and protein levels were measured in normoxic and hypoxic (24 h, 0.2% O_2) 661W cells stably expressing shHif1, shHif2 or shCtrl (Fig. 2B, C). *Hif1a* mRNA expression was reduced by about 65% in both normoxic and hypoxic 661W-shHif1 cells

when compared to 661W-shCtrl cells while it remained at control levels in 661W-shHif2 cells (Fig. 2B). *Hif2a* expression was reduced by roughly 80% in normoxic and hypoxic 661W-shHif2 but not 661W-shHif1 cells. Interestingly, an 86% increase in *Hif2a* levels was observed in hypoxic 661W-shHif1 cells, suggesting a compensatory induction of *Hif2a* upon *Hif1a* knockdown in hypoxia. The hypoxic state of the cells was confirmed by the significantly increased expression level of solute carrier 2a1 (*Slc2a1,* alias *Glut1,* Fig. 2B), a gene primarily regulated by HIF1. The diminished but still measurable *Slc2a1* expression levels in hypoxic 661W-shHif1 cells indicated a strongly but not fully blocked HIF1 activity, which is expected after robust but not complete *Hif1a* gene silencing (Fig. 2B). Western blots confirmed increased HIF1A and HIF2A protein levels in hypoxic cells and their specific reduction by the corresponding shRNAs (Fig. 2C). Thus, the selected shRNAs efficiently downregulated *Hif1a* and *Hif2a* at both the mRNA and protein levels.

To simultaneously downregulate *Hif1a* in photoreceptors and *Hif2a* in the RPE *in vivo*, we cloned the corresponding shRNAs (Fig. S1) into miR-E scaffolds (20) that were placed in the 3'UTRs of GFP (shHif1) and mCherry (shHif2) in a single plasmid. Expression of GFP::shHif1 in photoreceptors was driven by the GRK1 (37) and of mCherry::shHif2 in the RPE by the VMD2 promoter (38) (Fig. 2D). Using a single vector to deliver the two specific shRNAs to different cell types allowed an efficient and precise intervention. A scrambled RNA sequence replaced shHif1 and shHif2 in the shCtrl vector. To compare the potency of this dual-acting AAV with single-acting AAVs, we generated two vectors that delivered either shHif1 to the photoreceptors or shHif2 to the RPE (Fig. 2D).

Targeted expression in photoreceptors and RPE of wild type mice

The AAVs carrying shHif or shCtrl were injected into the subretinal space of wild type mice (Fig. 3A) to test their potential toxicity for RPE and photoreceptor integrity. Two weeks after administration, the injection site was visible as a hyperreflective spot in the fundus (Fig. 3B,C; arrows). OCT scans taken at the injection site showed minor layer distortions likely attributable to retinal injury caused by needle penetration. Beyond the injection site, however,

tissue integrity was preserved in shCtrl- or shHif-treated areas, as shown by OCT scans through the optic nerve head, indicating that neither vector was toxic to retinal cells or the RPE (Fig. 3B,C). Fluorescence funduscopy showed widespread GFP- (as surrogate marker for shHif1 expression) and mCherry- (indicating shHif2 expression) positive areas surrounding the injection site (Fig. 3B,C). Retinal cross-sections collected at 3 weeks post-injection (wpi) showed GFP and mCherry signals localized to photoreceptors and the RPE, respectively (Fig. 3D,E). However, weak mCherry fluorescence was also detected in the neural retina close to the injection site. The signal was much less robust than in the RPE and decreased to undetectable levels with increasing distance from the injection site. Similarly, some GFP fluorescence was observed in the RPE. While this may be attributed to phagocytosis of shed GFP-positive outer segments by RPE cells, we cannot completely rule out expression of the GRK1-driven gene in the RPE, as it has been observed for AAV8 in macaque before (39). To evaluate the transduction perimeter, GFP and mCherry fluorescence was examined on retinal and RPE flatmounts at 3 wpi. The GFP-positive area covered approximately 40-50% of the total retina and closely matched the mCherry-positive area in the corresponding RPE both in size and position (Fig. 3F,G). This demonstrates successful delivery of the transgenes and efficient expression in their intended target cells.

Potential inflammation was assessed by immunofluorescence staining for allograft inflammatory factor 1 (IBA1, alias AIF1) on retina and RPE flatmounts, and in retinal cross-sections at 3 wpi (Fig. 3F,G, Fig. S3A). Whereas reactive (amoeboid) microglia and/or macrophages were detected in the retina close to the injection site, ramified resting microglia populated the surrounding tissue. RPE flatmounts presented few IBA1-positive cells only close to the injection site. The presence of microglia or macrophages in this area might have been caused by retinal detachment and scar formation after subretinal injection. Apart from the perturbations at the injection site, the transduced areas showed normal staining patterns for cone arrestin (ARR3) and beta-catenin (CTNB1) (Fig. S3B), indicating no apparent adverse effects on cone photoreceptors and RPE following AAV delivery. In addition, retinal morphology appeared normal at 22 wpi with no signs of degeneration or functional

impairment (Fig. 3H,I; Fig. S3C). Collectively, these findings demonstrate that the dual-acting AAV vector selectively transduced photoreceptors and RPE cells in a broad area and did not induce degenerative effects beyond the injection site.

Mouse models for AMD

Our therapeutic strategy centers on targeting the alpha subunits of HIF1 and HIF2 transcription factors, which are stabilized under reduced oxygen levels. Stabilization is initiated when the activity of HIF-prolyl hydroxylases decreases due to reduced availability of O_2 as substrate. Reduced hydroxylation of HIF1A and HIF2A prevents their recognition by the VHL protein complex and subsequent degradation by proteasomes allowing them to accumulate and function as transcription factors. This accumulation (and activation) of HIF1 and HIF2 is mimicked in *Rod*$^{\Delta Vhl}$ mice, which lack VHL in rods. These mice represent a pseudohypoxia model in which the hypoxic response is elicited in the presence of normal oxygen levels leading to photoreceptor degeneration (5, 12). The stabilization of HIF1A by the chemical prolyl hydroxylase inhibitor Rodaxustat resulted in comparable cell death (40) supporting the validity of the model. However, eyes of ageing individuals and those afflicted by AMD experience genuine hypoxia affecting both photoreceptors and the RPE. Thus, we established a second model by knocking out *Vegfa* in RPE cells of adult mice (*RPE*$^{\Delta Vegfa}$; Fig. 4A). As reported by others, the lack of VEGFA disrupts the homeostasis in the choriocapillaris leading to vasoconstriction in the choroid. This results in the development of true hypoxic conditions, including HIF activation, consequently causing RPE and photoreceptor degeneration (10, 41, 42). To generate a local phenotype, we delivered Cre recombinase to the nasal RPE of 28-day-old *Vegfa*$^{fl/fl}$ mice (23) by the subretinal injection of an AAV4 expressing Cre-P2A-eGFP under control of the VMD2 promoter (Table 2). Inactivation of *Vegfa* expression in the transduced RPE was verified by *in situ* hybridization, and transduction was confirmed by staining for Cre in the consecutive section at 3 wpi. RPE cells positive for *Vegfa* lacked Cre staining (non-transduced area) while RPE cells negative for *Vegfa* were positive for Cre protein (transduced area) (Fig. 4B). This mutually exclusive

expression pattern indicated an effective suppression of *Vegfa* in transduced RPE cells. Choroidal flatmounts stained for podocalyxin (PODXL), an endothelial cell marker, demonstrated a strong reduction of choroidal vessel density at 3 wpi (Fig. 4C). To quantify the phenotype, we analysed the staining pattern of PODXL in sections through control and transduced regions lacking *Vegfa* expression. Transduced areas showed notable gaps in the PODXL pattern and a significant increase in the gap size (Fig. 4C), suggesting a collapse of the choriocapillaris and rearrangement of endothelial cells in the absence of RPE-derived VEGFA.

At 3 wpi the transduced area was clearly visible as a brighter region in the fundus that correlated with the GFP-positive area and thus expression of Cre (Fig. 4D). Angiography indicated a predominantly regular retinal vasculature, and OCT showed normal retinal thickness, with the expected small perturbations around the injection site at this time (Fig. 4D, upper panel). At 39 wpi, however, the same eye presented various abnormalities including fundus discoloration, RPE hypertrophy, retinal thinning with an almost complete loss of the ONL and vascular leakage (Fig. 4D-F; Fig. S4). The weak GFP signal (Fig. 4D) suggested either a loss of transgene expression or the death of transduced cells at this time point. To quantify the effect *in vivo*, we employed OCT volume scans and measured the ONL thickness in two nasal subfields. Direct comparisons showed a significantly reduced ONL thickness in $RPE^{\Delta Vegfa}$ but not in non-injected ($Vegfa^{fl/fl}$) or control-injected ($Vegfa^{fl/fl}$ *+PBS or +GFP)* mice (Fig. 4E). Light microscopy and quantification of equatorial nasal-temporal sections supported the *in vivo* findings and revealed significant thinning of the ONL and reduced length of PS that was restricted to the transduced nasal retina of $RPE^{\Delta Vegfa}$ mice (Fig. 4F,G). The phenotype was not caused by subretinal injections or the activity of the VMD2 promotor *per se* since the respective controls showed no signs of retinal degeneration (Fig. 4F,G) even though minor irregularities were occasionally detected in the RPE of some eyes injected with an AAV expressing eGFP under control of the VMD2 promoter ($Vegfa^{fl/fl}$ + GFP; Fig. 4E, Table 2).

Dual-acting anti-HIF gene therapy restores tissue integrity in *Rod*$^{\Delta Vhl}$ mice

Having validated the expression pattern and safety of the shHif AAV vector in wt mice (Fig. 3), we proceeded to investigate whether this vector can effectively interfere with the hypoxia pathway in our two mouse models. We first used the *Rod*$^{\Delta Vhl}$ mouse with its chronically activated molecular response to hypoxia in rod photoreceptors due to the rod-specific deletion of *Vhl* (Fig. 5A). The model is characterized by a HIF1-dependent, late onset progressive loss of photoreceptors, occasional disturbances in the RPE, and a decline in visual function (5, 12). As expected, untreated 26-week-old *Rod*$^{\Delta Vhl}$ mice showed patches of photoreceptor cell loss in the fundus, as well as RPE and photoreceptor irregularities in OCT images (Fig. 5B). Age-matched *Rod*$^{\Delta Vhl}$ mice injected with shCtrl vector displayed comparable phenotype at 22 wpi, with patches of degenerated areas in normal fundus that were prominently visible as dark flecks in fundus fluorescence images capturing vector-derived GFP and mCherry signals. In contrast, fundi and OCT images of shHif-treated animals displayed fewer irregularities and no obvious signs of RPE disturbances (Fig. 5B). To quantify the extent of rescue *in vivo*, we measured ONL thickness in the different groups using volumetric OCT scans. Although not reaching the thickness of control *Vhl*$^{fl/fl}$ mice (without Opsin-Cre), treatment of *Rod*$^{\Delta Vhl}$ mice with shHif resulted in a significantly thicker ONL compared to *Rod*$^{\Delta Vhl}$ mice treated with shCtrl (Fig. 5C). Light microscopy of retinal morphology at 22 wpi supported these findings and showed that retinal areas that had received the shHif virus had less severe ONL thinning and RPE disturbances than non- or shCtrl-transduced areas (Fig. 5D).

Gene expression analysis at 22 wpi showed reduced *Hif1a* but not *Hif2a* mRNA levels in the retina, (Fig. 5E) and reduced *Hif2a* but not *Hif1a* expression in the eyecup tissue that includes the RPE (Fig. 5F). This suggests a high degree of cell-type specificity of our dual-acting shHif gene silencing approach. The rather moderate reduction of the respective expression levels of *Hif1a* and *Hif2a* by only 20-30% was not surprising because tissue samples used for these experiments also contained cells from the transduced area that were

not targeted by our vector (e.g. 2nd and 3rd order neurons) and cells from non-transduced areas. This may also be the reason why levels of *Casp1* (marker for degenerative processes) and *Pde6b* (marker for rod integrity) in the retina and of *Rpe65* (marker for RPE integrity) in the eyecup were only slightly reduced or increased, respectively (Fig. 5E). Together with the significant rescue of retinal thickness our gene expression data collectively supports a considerable potential of the shHif approach for alleviating the harmful effects of a chronic hypoxic response in photoreceptors.

Dual-acting anti-HIF gene therapy restores tissue integrity in *RPE*$^{\Delta Vegfa}$ mice

We proceeded to assess the potential of the shHif approach to mitigate the degenerative effects of true chronic hypoxia in the *RPE*$^{\Delta Vegfa}$ model. Since this model also includes the pathogenic activation of HIF2A in the RPE (10), we compared the efficacy of the dual-acting shHif with single-acting shHif1 (targeting photoreceptors) and shHif2a (targeting the RPE) AAVs. Subretinal co-injections of AAV::VMD2-Cre-P2A-eGFP to inactivate *Vegfa* in the RPE, along with either shCtrl, shHif, shHif1 or shHif2 were performed at 4 weeks of age followed by analysis at 39 wpi. Funduscopy and OCT of *RPE*$^{\Delta Vegfa}$ mice injected with shCtrl showed discolored patches and affected tissue layers, indicating RPE disturbances and degeneration at 39 wpi (Fig. 6A), a phenotype similar to untreated *RPE*$^{\Delta Vegfa}$ mice (Fig 4D). In contrast, shHif-treated animals displayed only minor disturbances around the injections site, but no obvious retinal degeneration (Fig. 6A). The rescue effect by the treatment with the various viruses was quantified *in vivo* using OCT volume scans. Treatment with the dual-acting shHif virus preserved ONL thickness in *RPE*$^{\Delta Vegfa}$ mice significantly better than treatment with the single-acting or control AAVs. (Fig. 6B). The superior rescue effect by shHif was further verified by light microscopy of retinal sections (Fig. 6C) and measurements of ONL thickness and PS length (Fig. 6D) in a subset of mice. Eyes treated with shCtrl displayed a drastic thinning of the ONL, loss of PS, and variable thickness of the RPE in transduced areas. In contrast, mice treated with shHif had preserved PS with few disturbances, a thicker ONL, and only sporadic regions with irregular RPE morphology. shHif1 and shHif2 viruses rescued

the phenotype at intermediate levels (Fig. 6C,D). Areas that were not transduced by the Cre-expressing virus and thus with regular *Vegfa* expression in the RPE showed normal retinal morphologies for all injected eyes. The superior rescue effect by the dual-acting shHif virus underscores the importance of simultaneously targeting Hif1 in photoreceptors and Hif2 in the RPE to efficiently mitigate the consequences of chronic hypoxia. The dual-targeting approach was not only superior to targeting individual HIF transcription factors but was also long lasting and protected tissue integrity at least up to 61 wpi (Fig. 7). While $RPE^{\Delta Vegfa}$ mice treated with shCtrl exhibited significant loss of GFP and mCherry fluorescence when compared to 4 wpi, shHif treated mice still showed strong fluorescence suggesting preservation of photoreceptors and RPE (Fig. 7A,B). This was confirmed by light microscopy of retinal sections and quantification of ONL thickness and PS length which showed strong preservation of retinal morphology in shHif but not shCtrl treated mice (Fig 7C,D). The eyes injected with the GFP control virus provided a baseline for non-degenerated retinas allowing to assess the overall efficacy of the dual-acting shHif virus. Our findings demonstrate the long-term efficacy of shHif in preserving retinal structures by counteracting a chronic hypoxic response. In summary, the dual-acting gene therapy efficiently prevented photoreceptor loss and RPE alterations in two models of hypoxia-induced retinal degeneration, indicating its potential for a translation into a clinical setting.

Discussion

Age is the major non-genetic risk factor for the development of AMD. The aging ocular tissue undergoes several changes that result in reduced oxygen levels in the outer retina and increased expression of HIF target genes (1, 2, 5). Some HIF target genes, such as VEGFA and ANGPTL4, are angiogenic factors that ultimately contribute to the development of neovascular AMD (31, 32). Others, such as SERPINE1, may facilitate disease development by remodeling the extracellular matrix (30) or through their connection to senescence and ageing (43). Expression of all three hypoxia-related genes was increased in old donor eyes.

In addition, a hypoxic environment triggers an intracellular response that adjusts major metabolic pathways, including glycolysis, oxidative phosphorylation, lipid metabolism and others, to the new environmental condition. Such a metabolic shift likely contributes to cell death in the delicate photoreceptor neurons and the RPE, highlighting the complex interplay between ageing, hypoxia and cellular responses involved in AMD development (5, 10, 44–46). Thus, targeting the hypoxia pathway could serve as a mutation-independent therapeutic approach that may be beneficial for a wide range of patients affected by wet or dry AMD. Here we established an efficient RNA interference strategy that simultaneously targets HIF1 in the photoreceptors and HIF2 in the RPE. This dual-acting approach prevented retinal degeneration connected to a chronic hypoxic response in two mouse models of pseudo- or genuine hypoxia. Another key finding was the demonstration that this dual-acting gene therapy proved to be more effective than single-target treatments. This finding highlights the potential and superiority of multi-target therapies for complex multifactorial diseases such as AMD.

The use of shRNAs driven by Pol-II promoters to downregulate target genes has several advantages. The system allows targeting those cell types that require treatment without affecting other cells. In contrast to the transient effects of short-lived synthetic siRNAs, it also ensures long-lasting effects through continuous expression of the therapeutic RNAs for at least 61 weeks as illustrated by the sustained presence of the surrogate GFP and mCherry fluorescent proteins (Fig. 7). It also minimizes the possibility that a bolus injection of siRNAs overwhelms the endogenous RNAi pathway leading to toxic side effects (19, 47). Furthermore, this system is based on a single AAV vector and does not rely on double transduction of individual cells, trans-splicing, or other mechanisms that may reduce efficiency. The therapeutic approach is not only safe, but also potent and has protected tissue integrity in two different models of hypoxia-related retinal degeneration that share key aspects of AMD.

In contrast to our data for the chronic models presented here, the recent work of Babapoor-Farrokhran and colleagues suggests a beneficial function of HIF1 for the survival of

photoreceptors (48). However, this was concluded after induction of acute oxidative stress by $NaIO_3$ that may less accurately model the effects of a long-lasting chronic hypoxic response or environment. In addition, the chemicals used in their study can be toxic to photoreceptors *per se* (digoxin; (49)) or exhibit side effects apart from HIF activation (DMOG; (50, 51)). Nevertheless, data from their acute model is interesting and may best be correlated to the protective effects of hypoxic preconditioning against acute light-induced retinal degeneration (52). Since this indicates that acute and chronic hypoxic responses have distinct consequences for retinal cells, we believe that our two genetic models for chronic hypoxia represent the situation in the aged eye more accurately than drug-induced acute models.

While the *Rod*$^{\Delta Vhl}$ model has chronically active HIFs in normoxic rods causing HIF1-dependent photoreceptor degeneration (5), the RPE-specific deletion of *Vegfa* in the *RPE*$^{\Delta Vegfa}$ model affects the choroidal vasculature, leading to true tissue hypoxia and HIF2-dependent RPE and retinal degeneration (10). Since the true tissue hypoxia in *RPE*$^{\Delta Vegfa}$ mice affects several cell types and elicits broad effects including changes in metabolism (10), *RPE*$^{\Delta Vegfa}$ mice may better represent the complex, multifactorial environment in the aging eye. To knockdown *Vegfa* in adult RPE cells, we delivered a VMD2-controlled Cre transgene to *Vegfa*$^{fl/fl}$ mice. This approach is more specific, efficient and reproducible compared to methods suffering from variable and patchy Cre expression in RPE of transgenic mice (42, 53) or the lack of cell type specificity after delivery of CjCas9 for indel generation (41).

The therapeutic vector was designed to express shHif1 in photoreceptors and shHif2 in the RPE with GFP and mCherry as surrogate markers. Despite expression of GFP::shHif1 was controlled by the GRK1 promotor, GFP fluorescence was also visible in the RPE (Fig. 3D,E). This was likely due to phagocytosis of photoreceptor material by the RPE, or to some expression of the gene in the RPE following delivery by AAV8, which has a known tropism for the RPE, as observed in macaque studies (39). This opens the possibility that some molecules targeting *Hif1a* mRNA reached the RPE. Although phagocytosed material would likely be confined to lysosomes, we cannot exclude some downregulation of *Hif1a* transcripts in the RPE by such ‘spills’. However, since the knockout of *Hif1a* in the mouse RPE does not

cause phenotypic changes (42) this possibility does not significantly influence validity, specificity and efficacy of our approach.

Although our dual-active gene therapy rescued the phenotype in both mouse models, our results suggest a higher efficiency in *RPE*$^{\Delta Vegfa}$ mice where degeneration is based on true hypoxia due to pathological changes in the choroidal vasculature (Fig. 4C). The RNA-induced silencing complex (RISC) that is formed after shRNA expression reduces stability or translation of mRNA transcripts but does not affect preformed proteins. Thus, the efficacy of shRNA-mediated downregulation of protein activity depends on the expression levels of target RNA. Considering reports suggesting that hypoxia can reduce levels and half-lives of *Hif1a* and *Hif2a* transcripts (54, 55), it appears possible that RNA interference is more effective in the model of real hypoxia due to lower levels of target mRNAs. Clearly, unraveling the mechanisms that contribute to the differences in treatment efficacies in the two models needs further research and is important to improve the RNA interference approach even further. A limitation of our study lies in structural differences between the mouse and the human retina. Unlike humans, mice do not possess a macula which prevents our models from presenting all aspects of AMD. However, since the molecular response to hypoxia with the activation of HIF transcription factors is quite universal, we nonetheless believe that our therapeutic approach targeting this conserved mechanism is translatable to the human situation.

Conclusion

Since a reduction of oxygen delivery to the outer retina through the choroidal system affects both RPE and photoreceptors, it is important that a therapeutic intervention targets the degeneration-causing factors in both cell types simultaneously and specifically. We approached this requirement through the dual-active gene therapy system using a single AAV. Delivery of therapeutic genes by AAV is safe and has been evaluated in several clinical trials (56, 57). The first FDA and EMA-approved gene therapy (Luxturna©) for Leber

congenital amaurosis type 2 not only supports the safety but also the efficacy of the delivery of genetic material to target cells by subretinal AAV injections. The approach presented here further expands the potential of AAVs as a therapeutic system by using a single AAV vector with two specific Pol-II promotors to drive expression of shRNAs targeting two transcripts in two distinct cell types. We believe that the system demonstrates potential for widespread applicability to other multifactorial diseases that necessitate modifications of gene expression across various cell types or tissues. Since RNAi-based therapeutics, including siRNA and shRNA, have already been used in several clinical trials, e.g., to target cancer or genetic disorders (58, 59), the system developed here may be translated for the use in patients, particularly for the treatment of retinal disorders associated with a chronic hypoxic response such as AMD.

List of abbreviations

AAV: adeno-associated virus
AMD: age-related macular degeneration
ARR3: cone arrestin
BM: Bruch's membrane
CC: choriocapillaris
CTNB1: beta-catenin
Ctrl: control
DAPI: 4',6-diamidino-2-phenylindole
ERG: electroretinogram
Fl: flox
GCL: ganglion cell layer
GFP: green fluorescent protein
GRK1: G-protein coupled kinase 1
HIF: hypoxia-inducible factor
IBA1: allograft inflammatory factor 1
INL: inner nuclear layer
OCT: optical coherence tomography
ONL: outer nuclear layer

PFA: paraformaldehyde
PODXL: podocalyxin
PS: photoreceptor segment
VEGFA: vascular endothelial growth factor A
RPE: retinal pigment epithelium
siRNA: small interfering RNA
shRNA: small hairpin RNA
VHL: von Hippel Lindau
VMD2: vitelliform macular dystrophy 2
WPI: weeks post injection
3'UTR: 3' untranslated region

Declarations

Ethics approval and consent to participate

Analysis of human ocular tissue was approved by the Cantonal Ethic Commission (license numbers BASEC-Nr: PB_2017-00550 and 2020-01856) and adhered to the tenets of the Declaration of Helsinki. Animal experimentation was approved by the Cantonal Veterinary Office of Zürich, Switzerland (license numbers: ZH019/2019 and ZH105/2022) and adhered to the ARVO statement for the use of Animals in Ophthalmic and Vision Research.

Consent for publication

Not applicable

Availability of data and materials

All data generated or analyzed during this study are included in this article and its supplementary information files.

Competing interest

The authors declare that they have no competing interests.

Funding

This work was supported by Swiss National Science Foundation grants 31003A 173008 and 310030 200798, and a research grant of the University of Zürich to L.E. (FK-20-028).

Authors' contributions

L.E. M.S. and C.G. conceived the study. L.E. designed and performed experiments and the analysis. I.M and F.B. collected human ocular tissue. M.S.; C.I.; D.S.; F.P; E.K.; A.W.; D.F.; L.M.; G.W.; I.T., L.G., SL.B.; SE.B. contributed to data collection and performed experiments. All authors contributed to project design, organization of the experiments, interpretation of results. L.E., M.S. and C.G wrote the manuscript. All authors read and approved the final manuscript.

Acknowledgements

The Viral Vector Facility (VVF) of the Neuroscience Center Zurich (ZNZ) produced all AAVs and the Laboratory Animal Services Center (LASC) of the University of Zurich was responsible for animal care.

Figure legends

Figure 1 | Gene expression in the human retina and RPE. Expression of *VEGFA* **(A)**, *ANGPTL4* **(B)**, *SERPINE1* **(C)** *CFH* **(D)** and *GNAT2* **(E)** was determined by real-time PCR in the young (Y) and old (O) peripheral (P; red dots) and central (C; blue dots) retina and RPE of human donor eyes without known ocular pathology (left and middle panels) or diagnosed with AMD (right panels). For the comparison of P with C, data points from both young and old donors were combined (middle panels). For the comparison of AMD with normal age-matched donors (green dots), data points from both the periphery and center were combined (right panels). Shown are means (line) and individual values on a log10 scale (y-axis).

Outliers were identified and excluded using Grubbs method, and significance was determined by unpaired t-tests. N = 13-15 per group. **(F)** Graphical representation of the regions collected for analysis. * marks the macular region.

Figure 2 | *In vitro* validation of *Hif1a* and *Hif2a* shRNAs and design of the dual-acting AAV vector. (A) Graphical representation of tissue changes leading to hypoxia and degenerative processes during aging and AMD. **(B)** Gene expression analysis of 661W cells stably expressing shCtrl, shHif1 or shHif2 after normoxic or hypoxic (24 h, 0.2% O_2) exposure. Values were normalized to beta Actin (*Actb*) and expressed relatively to normoxic 661W-shCtrl (set to 1). Shown are individual values (n=3) and means ± SD. Significance was tested using a one-way ANOVA with Tukey's multiple comparison test. *: statistically significant; p-values of all comparisons are given in Table S1. **(C)** Western blot analysis for HIF1A, HIF2A and ACTB in 661W cells stably expressing shCtrl, shHif1 or shHif2 after normoxic and hypoxic exposure. **(D)** Schematic representation of the DNA constructs packaged into AAV vectors. AAV-shHif: the construct consists of the GRK1 promotor driving photoreceptor-specific expression of shHif1a embedded in the miR-E scaffold in the 3'UTR of GFP, followed by the VMD2 promotor controlling RPE-specific expression of shHif2a embedded in the miR-E scaffold in the 3'UTR of mCherry. AAV-shCtrl: a scrambled non-targeting control shRNA sequence replaced shHif1a and shHif2a. AAV-shHif1: the GRK1 promotor drives photoreceptor-specific expression of shHif1a embedded in the miR-E scaffold in the 3'UTR of GFP. AAV-shHif2: the VMD2 promotor controls RPE-specific expression of shHif2a embedded in the miR-E scaffold in the 3'UTR of mCherry. Sequences of shRNAs are provided in Fig. S1 and supplemental data SD1. CC: choriocapillaris, BM: Bruch`s membrane, RPE: retinal pigment epithelium, PS: photoreceptor segments, ONL: outer nuclear layer.

Figure 3 | Pattern and safety of shHif transgene expression in wt mice after AAV-mediated delivery. (A) Illustration of transvitreal AAV-delivery to the subretinal space

targeting photoreceptor cells (shown in green due to GFP) and RPE cells (shown in red due to mCherry). **(B, C)** Funduscopy, OCT scans and fundus fluorescence of wt mice injected with shCtrl (B) or shHif (C) at 2 wpi. Orange and red lines in the fundus images indicate positions of the respective OCT scans. Fluorescence indicates transduced areas in the retina (green, GFP) and RPE (red, mCherry). White arrows: injection site, *: optic nerve head. **(D, E)** Retinal cross-sections of wt mice injected with shCtrl (D) or shHif (E) at 3 wpi. Green/white: GFP-positive photoreceptors / RPE. Red/white: mCherry-positive RPE cells. Shown are merged images (left) and individual fluorescence channels (middle and right). **(F, G)** Retina and their corresponding RPE flatmounts from wt mice injected with shCtrl (F) or shHif (G) at 3 wpi. Shown are native GFP (green) and mCherry (red) fluorescence and stainings for IBA1 (white). Boxed areas in the fluorescence images are shown in higher magnification (middle). Arrow: injection site. **(H)** Representative retinal morphologies of wt mice injected with shCtrl (left) or shHif (right) at 22 wpi. **(I)** Scotopic and photopic electroretinograms (ERG) of wt mice injected with shCtrl (grey) or shHif (orange) at 22 wpi. Shown are scotopic a- and b-wave and photopic b-wave amplitudes as a function of stimulus intensity. Shaded areas indicate SD, n=4 per group. Scale bars: as indicated. RPE: retinal pigment epithelium, PS: photoreceptor segments, ONL: outer nuclear layer, INL: inner nuclear layer, GCL: ganglion cell layer, SRS: subretinal space.

Figure 4 | Assessment of the *RPE$^{\Delta Vegfa}$* phenotype. (A) Graphical representation of the *RPE$^{\Delta Vegfa}$* model in which deletion of *Vegfa* in the RPE leads to reduced choroidal vessel density, RPE alterations and photoreceptor degeneration. **(B)** *In situ* hybridization for *Vegfa* (red) and immunofluorescence for Cre (magenta) in areas that were or were not transduced with AAV::VMD2-Cre-P2A-eGFP. **(C)** Immunofluorescence for PODXL expression in choroidal vascular endothelial cells in non-transduced (left) and transduced (right) areas of the same eye. Top panels: choroidal flatmounts. Middle panels: original stainings for PODXL in choroidal cross-sections (top), corresponding contrast-enhanced threshold images (middle) used for pixel intensity scans for quantification (bottom). Right panel: Quantification

of pixel intensity scans in transduced (blue) and non-transduced (grey) areas of *RPE*$^{\Delta Vegfa}$ mice at 39 wpi. Pixels of zero intensity (indicating gaps between PODXL-positive cells) were summed over a distance of 250 µm and shown as individual values. 18-19 measurements in n=3 eyes. Unpaired t-test. **(D)** Funduscopy, OCT scans, fundus fluorescence and angiography of *RPE*$^{\Delta Vegfa}$ mice at 3 (top) and 39 (bottom) wpi. Orange and red lines in the fundus images indicate positions of the respective OCT scans that are shown in lower and higher magnifications. Green fluorescence in GFP-labelled panels indicates presence of Cre at 3 wpi, while predominantly background fluorescence was visible at 39 wpi. Fluorescence angiographies suggested intact (3 wpi) or leaky (39 wpi) retinal vessels. Arrows: injection site, *: optic nerve head. **(E)** Color-coded ONL thickness maps of *Vegfa*$^{fl/fl}$, *RPE*$^{\Delta Vegfa}$, *Vegfa*$^{fl/fl}$ + PBS and *Vegfa*$^{fl/fl}$ + GFP mice generated from OCT volume scan at 39 wpi. Grids were aligned to the optic nerve (ON) and the ONL thickness was recorded in the two nasal subfields (marked by the orange line) and indicated with numbers (artificial units). Right panel: boxplots of ONL thickness in the two nasal subfields in mice as indicated. Shown are average values of individual eyes (dots) and means of all eyes (line). Note: values for control injected mice (*Vegfa*$^{fl/fl}$ + PBS and *Vegfa*$^{fl/fl}$ + GFP) were combined. n=4 (*Vegfa*$^{fl/fl}$); n=11 (*RPE*$^{\Delta Vegfa}$); n=6 (*Vegfa*$^{fl/fl}$ + GFP / *Vegfa*$^{fl/fl}$ + PBS). One-way ANOVA with Tukey's multiple comparison test. P-values as shown. **(F)** Representative retinal morphologies of *Vegfa*$^{fl/fl}$ mice (left) that were subretinally injected with AAVs expressing Cre (*RPE*$^{\Delta Vegfa}$) or GFP (*Vegfa*$^{fl/fl}$ + GFP), or with PBS (*Vegfa*$^{fl/fl}$ + PBS) at 39 wpi. **(G)** Quantification of ONL thickness and PS length. Shown are spidergrams and average values in the transduced nasal area (400-2000 µm from the optic nerve head (ON)) of *Vegfa*$^{fl/fl}$ (black), *RPE*$^{\Delta Vegfa}$ (blue), *Vegfa*$^{fl/fl}$ + GFP (purple), and *Vegfa*$^{fl/fl}$ + PBS (yellow) mice at 39 wpi. Shown are means ± SD and individual data points. n=3 (*Vegfa*$^{fl/fl}$; *Vegfa*$^{fl/fl}$ + GFP; *Vegfa*$^{fl/fl}$ + PBS); n=2 (*RPE*$^{\Delta Vegfa}$). One-way ANOVA with Tukey's multiple comparison test, p-values as indicated. CC: choriocapillaris, BM: Bruch's membrane, RPE: retinal pigment epithelium, PS: photoreceptor segments, ONL: outer nuclear layer, INL: inner nuclear layer, GCL: ganglion cell layer.

Figure 5 | Rescue of the *Rod*$^{\Delta Vhl}$ phenotype by the dual-acting AAV therapy. (A) Schematic representation of *Rod*$^{\Delta Vhl}$ mice and rescue of RPE (red) and photoreceptors (green) through downregulation of *Hif2a* in the RPE and *Hif1a* in photoreceptors by shHif. **(B)** Funduscopy, OCT scans and fundus fluorescence assessed at 26 weeks of age (22 wpi) in *Rod*$^{\Delta Vhl}$ mice that were either non-injected (left) or treated with shCtrl (middle) or shHif (right). Orange and red lines in the fundus images indicate positions of the respective OCT scans. OCT scans of higher magnifications are included. Fundus fluorescence images (last two rows) show the transduced areas in the retina (green, GFP) and RPE (red, mCherry). *: optic nerve head. **(C)** Color-coded ONL thickness maps of *Vhl*$^{fl/fl}$, *Rod*$^{\Delta Vhl}$ + shCtrl and *Rod*$^{\Delta Vhl}$ + shHif mice generated from OCT volume scans at 22 wpi. Grids were aligned to the optic nerve (ON). The ONL thickness was measured in seven subfields and indicated with numbers (artificial units). Right panel: quantification of ONL thickness in the seven subfields (outlined by the orange line in the grid). Shown are average values of the subfields in individual eyes (dots) and means of all eyes (line) in box blots (n≥9). One-way ANOVA with Tukey's multiple comparison test. P-values as shown. **(D)** Representative retinal morphologies of transduced regions of *Vhl*$^{fl/fl}$ control and *Rod*$^{\Delta Vhl}$ mice injected with shCtrl or shHif. All mice were 26 weeks of age (22 wpi) at time of analysis. **(E, F)** Relative gene expression levels in retinas (E) or eyecups (F) of *Rod*$^{\Delta Vhl}$ + shCtrl (grey) and *Rod*$^{\Delta Vhl}$ + shHif (orange) mice at 22 wpi. Expression was normalized to beta-actin (*Actb*) and shown relative to expression in *Rod*$^{\Delta Vhl}$ + shCtrl mice (set to 1). Shown are means ± SD of n = 11-12. Unpaired t-test. P-values as indicated. RPE: retinal pigment epithelium, ONL: outer nuclear layer, INL: inner nuclear layer, GCL: ganglion cell layer.

Figure 6 | Rescue of the *RPE*$^{\Delta Vegfa}$ phenotype by the dual-acting AAV therapy

(A) Funduscopy, OCT scans and fundus fluorescence of *RPE*$^{\Delta Vegfa}$ mice injected with shCtrl (left) or shHif (right) at 39 wpi. Orange and red lines in the fundus images indicate positions of the respective OCT scans that are shown in lower and higher magnifications. Fundus fluorescence indicates transduced areas in the retina (green, GFP) and RPE (red, mCherry).

*: optic nerve head. **(B)** Color-coded ONL thickness maps generated from OCT volume scans of *RPE*$^{\Delta Vegfa}$ + shCtrl, *RPE*$^{\Delta Vegfa}$ + shHif, *RPE*$^{\Delta Vegfa}$ + shHif1 and *RPE*$^{\Delta Vegfa}$ + shHif2 mice at 39 wpi. Grids were aligned to the optic nerve (ON). The ONL thickness was measured in the two nasal subfields (outlined by the orange line in the grid) that were most affected in *RPE*$^{\Delta Vegfa}$ mice and indicated with numbers (artificial units). Right panel: quantification of ONL thickness in the nasal two subfields. Shown are average values in individual eyes (dots) and means of all eyes (line) in box blots. n=11 (shCtrl, shHif); n=9 (shHif1); n=8 (shHif2). One-way ANOVA with Dunnett's multiple comparison test comparing all groups to shHif. p-values as shown. **(C)** Representative retinal morphologies of transduced and non-transduced areas of *RPE*$^{\Delta Vegfa}$ mice treated with AAVs as indicated. Analysis was at 39 wpi. **(D)** Quantification of ONL thickness and PS length of the four treatment groups. Shown are spidergrams and average values of the transduced nasal area (400-2000 µm from the optic nerve head (ON)) of a subset of mice that were already analyzed by volume scans (B) at 39 wpi. Grey: shCtrl; orange: shHif; green shHif1; blue: shHif2. Shown are means ± SD and individual data points. One-way ANOVA with Dunnett's multiple comparison test comparing all groups to shHif. P-values as shown. shHif: n=4 (ONL) and n=3 (PS); shHif1: n=9 (ONL) and n=4 (PS); shHif2: n=8 (ONL) and n=6 (PS); shCtrl: n=2 (ONL and PS). RPE: retinal pigment epithelium, PS: photoreceptor segments, ONL: outer nuclear layer, INL: inner nuclear layer, GCL: ganglion cell layer, BM: Bruch's membrane.

Figure 7 | Long-lasting rescue of the *RPE*$^{\Delta Vegfa}$ phenotype by the dual-acting AAV therapy

(A, B) Funduscopy and fundus fluorescence of *RPE*$^{\Delta Vegfa}$ mice injected with shCtrl (top) or shHif (bottom) analyzed at 4 wpi (A) and 61 wpi (B). Fluorescence indicates transduced areas in the retina (green, GFP) and RPE (red, mCherry). *: optic nerve head. **(C)** Representative retinal morphologies of transduced and non-transduced areas of *RPE*$^{\Delta Vegfa}$ mice injected with shCtrl or shHif, analyzed at 61 wpi. **(D)** Quantification of ONL thickness and PS length at 61 wpi, presented as spidergrams (left) and boxplots (right) presenting the

averaged values of the transduced nasal area (400-2000 µm from the optic nerve head (ON)). Treatment groups: *Vegfa*$^{flox/flox}$ mice injected with GFP control virus (green), *RPE*$^{\Delta Vegfa}$ + shHif mice (orange) and *RPE*$^{\Delta Vegfa}$ + shCtrl mice (grey) at 61 wpi. Note: ONL thickness and PS length in *RPE*$^{\Delta Vegfa}$ + GFP mice are not shown in spidergrams to reduce complexity of the figure panels. Shown are means ± SD and individual data points. One-way ANOVA with Tukey's multiple comparison tests. P-values as shown. shHif: n=11 (ONL) and n= 9 (PS); shCtrl: n=10 (ONL) and n=6 (PS); GFP: n=3 (ONL and PS).

References

1. Grunwald, JE, Metelitsina, TI, Dupont, JC, Ying, GS, Maguire, MG. Reduced foveolar choroidal blood flow in eyes with increasing AMD severity. *Invest Ophthalmol Vis Sci*. 2005;46(3):1033–1038.
2. Berenberg, TL, Metelitsina, TI, Madow, B, Dai, Y, Ying, GS, Dupont, JC, Grunwald, L, Brucker, AJ, Grunwald, JE. The association between drusen extent and foveolar choroidal blood flow in age-related macular degeneration. *Retina*. 2012;32(1):25–31.
3. Ramrattan, RS, van der Schaft, TL, Mooy, CM, de Bruijn, WC, Mulder, PG, de Jong, PT. Morphometric analysis of Bruch's membrane, the choriocapillaris, and the choroid in aging. *Invest Ophthalmol Vis Sci*. 1994;35(6):2857–2864.
4. Wakatsuki, Y, Shinojima, A, Kawamura, A, Yuzawa, M. Correlation of Aging and Segmental Choroidal Thickness Measurement using Swept Source Optical Coherence Tomography in Healthy Eyes. *PLoS One*. 2015;10(12):e0144156.
5. Barben, M, Ail, D, Storti, F, Klee, K, Schori, C, Samardzija, M, Michalakis, S, Biel, M, Meneau, I, Blaser, F, Barthelmes, D, Grimm, C. Hif1a inactivation rescues photoreceptor degeneration induced by a chronic hypoxia-like stress. *Cell Death Differ*. 2018;25(12):2071–2085.
6. Mullins, RF, Johnson, MN, Faidley, EA, Skeie, JM, Huang, J. Choriocapillaris vascular dropout related to density of drusen in human eyes with early age-related macular degeneration. *Invest Ophthalmol Vis Sci*. 2011;52(3):1606–1612.
7. Bressler, SB, Maguire, MG, Bressler, NM, Fine, SL. Relationship of drusen and abnormalities of the retinal pigment epithelium to the prognosis of neovascular macular degeneration. The Macular Photocoagulation Study Group. *Arch Ophthalmol*. 1990;108(10):1442–1447.
8. Pauleikhoff, D, Harper, CA, Marshall, J, Bird, AC. Aging changes in Bruch's membrane. A histochemical and morphologic study. *Ophthalmology*. 1990;97(2):171–178.
9. Bhutto, I, Lutty, G. Understanding age-related macular degeneration (AMD): relationships between the photoreceptor/retinal pigment epithelium/Bruch's membrane/choriocapillaris complex. *Mol Aspects Med*. 2012;33(4):295–317.
10. Kurihara, T, Westenskow, PD, Gantner, ML, Usui, Y, Schultz, A, Bravo, S, Aguilar, E, Wittgrove, C, Friedlander, MS, Paris, LP, Chew, E, Siuzdak, G, Friedlander, M. Hypoxia-induced metabolic stress in retinal pigment epithelial cells is sufficient to induce photoreceptor degeneration. *Elife*. 2016;5
11. Somasundaran, S, Constable, IJ, Mellough, CB, Carvalho, LS. Retinal pigment epithelium and age-related macular degeneration: A review of major disease mechanisms. *Clin Exp Ophthalmol*. 2020;48(8):1043–1056.
12. Lange, C, Caprara, C, Tanimoto, N, Beck, S, Huber, G, Samardzija, M, Seeliger, M, Grimm, C. Retina-specific activation of a sustained hypoxia-like response leads to severe retinal degeneration and loss of vision. *Neurobiol Dis*. 2011;41(1):119–130.
13. Khan, AA, Betel, D, Miller, ML, Sander, C, Leslie, CS, Marks, DS. Transfection of small RNAs globally perturbs gene regulation by endogenous microRNAs. *Nat Biotechnol*. 2009;27(6):549–555.

14. Martin, JN, Wolken, N, Brown, T, Dauer, WT, Ehrlich, ME, Gonzalez-Alegre, P. Lethal toxicity caused by expression of shRNA in the mouse striatum: implications for therapeutic design. *Gene Ther*. 2011;18(7):666–673.
15. Snøve, O, Rossi, JJ. Toxicity in mice expressing short hairpin RNAs gives new insight into RNAi. *Genome Biol*. 2006;7(8):231.
16. Lee, Y, Ahn, C, Han, J, Choi, H, Kim, J, Yim, J, Lee, J, Provost, P, Rådmark, O, Kim, S, Kim, VN. The nuclear RNase III Drosha initiates microRNA processing. *Nature*. 2003;425(6956):415–419.
17. Silva, JM, Li, MZ, Chang, K, Ge, W, Golding, MC, Rickles, RJ, Siolas, D, Hu, G, Paddison, PJ, Schlabach, MR, Sheth, N, Bradshaw, J, Burchard, J, Kulkarni, A, Cavet, G, Sachidanandam, R, McCombie, WR, Cleary, MA, Elledge, SJ, Hannon, GJ. Second-generation shRNA libraries covering the mouse and human genomes. *Nat Genet*. 2005;37(11):1281–1288.
18. Bauer, M, Kinkl, N, Meixner, A, Kremmer, E, Riemenschneider, M, Förstl, H, Gasser, T, Ueffing, M. Prevention of interferon-stimulated gene expression using microRNA-designed hairpins. *Gene Ther*. 2009;16(1):142–147.
19. Gu, S, Jin, L, Zhang, Y, Huang, Y, Zhang, F, Valdmanis, PN, Kay, MA. The loop position of shRNAs and pre-miRNAs is critical for the accuracy of dicer processing in vivo. *Cell*. 2012;151(4):900–911.
20. Fellmann, C, Hoffmann, T, Sridhar, V, Hopfgartner, B, Muhar, M, Roth, M, Lai, DY, Barbosa, IA, Kwon, JS, Guan, Y, Sinha, N, Zuber, J. An optimized microRNA backbone for effective single-copy RNAi. *Cell Rep*. 2013;5(6):1704–1713.
21. Haase, VH, Glickman, JN, Socolovsky, M, Jaenisch, R. Vascular tumors in livers with targeted inactivation of the von Hippel-Lindau tumor suppressor. *Proc Natl Acad Sci U S A*. 2001;98(4):1583–1588.
22. Le, YZ, Zheng, L, Zheng, W, Ash, JD, Agbaga, MP, Zhu, M, Anderson, RE. Mouse opsin promoter-directed Cre recombinase expression in transgenic mice. *Mol Vis*. 2006;12:389–398.
23. Gerber, HP, Hillan, KJ, Ryan, AM, Kowalski, J, Keller, GA, Rangell, L, Wright, BD, Radtke, F, Aguet, M, Ferrara, N. VEGF is required for growth and survival in neonatal mice. *Development*. 1999;126(6):1149–1159.
24. Kay, CN, Ryals, RC, Aslanidi, GV, Min, SH, Ruan, Q, Sun, J, Dyka, FM, Kasuga, D, Ayala, AE, Van Vliet, K, Agbandje-McKenna, M, Hauswirth, WW, Boye, SL, Boye, SE. Targeting photoreceptors via intravitreal delivery using novel, capsid-mutated AAV vectors. *PLoS One*. 2013;8(4):e62097.
25. Storti, F, Klee, K, Todorova, V, Steiner, R, Othman, A, van der Velde-Visser, S, Samardzija, M, Meneau, I, Barben, M, Karademir, D, Pauzuolyte, V, Boye, SL, Blaser, F, Ullmer, C, Dunaief, JL, Hornemann, T, Rohrer, L, den Hollander, A, von Eckardstein, A, Fingerle, J, Maugeais, C, Grimm, C. Impaired ABCA1/ABCG1-mediated lipid efflux in the mouse retinal pigment epithelium (RPE) leads to retinal degeneration. *Elife*. 2019;8
26. Gasparini, SJ, Tessmer, K, Reh, M, Wieneke, S, Carido, M, Völkner, M, Borsch, O, Swiersy, A, Zuzic, M, Goureau, O, Kurth, T, Busskamp, V, Zeck, G, Karl, MO, Ader, M. Transplanted human cones incorporate into the retina and function in a murine cone degeneration model. *J Clin Invest*. 2022;132(12)
27. Geiger, P, Barben, M, Grimm, C, Samardzija, M. Blue light-induced retinal lesions, intraretinal vascular leakage and edema formation in the all-cone mouse retina. *Cell Death Dis*. 2015;6(11):e1985.
28. Ebner, LJA, Samardzija, M, Storti, F, Todorova, V, Karademir, D, Behr, J, Simpson, F, Thiersch, M, Grimm, C. Transcriptomic analysis of the mouse retina after acute and chronic normobaric and hypobaric hypoxia. *Sci Rep*. 2021;11(1):16666.
29. Tan, E, Ding, XQ, Saadi, A, Agarwal, N, Naash, MI, Al-Ubaidi, MR. Expression of cone-photoreceptor-specific antigens in a cell line derived from retinal tumors in transgenic mice. *Invest Ophthalmol Vis Sci*. 2004;45(3):764–768.
30. Biasella, F, Strunz, T, Kiel, C, On, BOTIAGCI, Weber, BHF, Friedrich, U. Vitronectin and Its Interaction with PAI-1 Suggests a Functional Link to Vascular Changes in AMD Pathobiology. *Cells*. 2022;11
31. Qin, Y, Dinabandhu, A, Cao, X, Sanchez, JC, Jee, K, Rodrigues, M, Guo, C, Zhang, J, Vancel, J, Menon, D, Khan, NS, Ma, T, Tzeng, SY, Daoud, Y, Green, JJ, Semenza, GL, Montaner, S, Sodhi, A. ANGPTL4 influences the therapeutic response of patients with neovascular age-related macular degeneration by promoting choroidal neovascularization. *JCI Insight*. 2022;7(13)
32. Witmer, AN, Vrensen, GF, Van Noorden, CJ, Schlingemann, RO. Vascular endothelial growth factors and angiogenesis in eye disease. *Prog Retin Eye Res*. 2003;22(1):1–29.

33. Meade, ES, Ma, YY, Guller, S. Role of hypoxia-inducible transcription factors 1alpha and 2alpha in the regulation of plasminogen activator inhibitor-1 expression in a human trophoblast cell line. *Placenta*. 2007;28(10):1012–1019.
34. Semenza, GL. Targeting HIF-1 for cancer therapy. *Nat Rev Cancer*. 2003;3(10):721–732.
35. McHarg, S, Clark, SJ, Day, AJ, Bishop, PN. Age-related macular degeneration and the role of the complement system. *Mol Immunol*. 2015;67(1):43–50.
36. Ronning, KE, Allina, GP, Miller, EB, Zawadzki, RJ, Pugh, EN, Herrmann, R, Burns, ME. Loss of cone function without degeneration in a novel Gnat2 knock-out mouse. *Exp Eye Res*. 2018;171:111–118.
37. Khani, SC, Pawlyk, BS, Bulgakov, OV, Kasperek, E, Young, JE, Adamian, M, Sun, X, Smith, AJ, Ali, RR, Li, T. AAV-mediated expression targeting of rod and cone photoreceptors with a human rhodopsin kinase promoter. *Invest Ophthalmol Vis Sci*. 2007;48(9):3954–3961.
38. Esumi, N, Oshima, Y, Li, Y, Campochiaro, PA, Zack, DJ. Analysis of the VMD2 promoter and implication of E-box binding factors in its regulation. *J Biol Chem*. 2004;279(18):19064–19073.
39. Crosson, SM, Bennett, A, Fajardo, D, Peterson, JJ, Zhang, H, Li, W, Leahy, MT, Jennings, CK, Boyd, RF, Boye, SL, Agbandge-McKenna, M, Boye, SE. Effects of Altering HSPG Binding and Capsid Hydrophilicity on Retinal Transduction by AAV. *J Virol*. 2021;95(10)
40. Nsiah, NY, Morgan, AB, Donkor, N, Inman, DM. Long-term HIF-1α stabilization reduces respiration, promotes mitophagy, and results in retinal cell death. *Sci Rep*. 2023;13(1):20541.
41. Kim, E, Koo, T, Park, SW, Kim, D, Kim, K, Cho, HY, Song, DW, Lee, KJ, Jung, MH, Kim, S, Kim, JH, Kim, JH, Kim, JS. In vivo genome editing with a small Cas9 orthologue derived from Campylobacter jejuni. *Nat Commun*. 2017;8:14500.
42. Kurihara, T, Westenskow, PD, Bravo, S, Aguilar, E, Friedlander, M. Targeted deletion of Vegfa in adult mice induces vision loss. *J Clin Invest*. 2012;122(11):4213–4217.
43. Eren, M, Boe, AE, Klyachko, EA, Vaughan, DE. Role of plasminogen activator inhibitor-1 in senescence and aging. *Semin Thromb Hemost*. 2014;40(6):645–651.
44. Todorova, V, Stauffacher, MF, Ravotto, L, Nötzli, S, Karademir, D, Ebner, LJA, Imsand, C, Merolla, L, Hauck, SM, Samardzija, M, Saab, AS, Barros, LF, Weber, B, Grimm, C. Deficits in mitochondrial TCA cycle and OXPHOS precede rod photoreceptor degeneration during chronic HIF activation. *Mol Neurodegener*. 2023;18(1):15.
45. McHugh, KJ, Li, D, Wang, JC, Kwark, L, Loo, J, Macha, V, Farsiu, S, Kim, LA, Saint-Geniez, M. Computational modeling of retinal hypoxia and photoreceptor degeneration in patients with age-related macular degeneration. *PLoS One*. 2019;14(6):e0216215.
46. Stefánsson, E, Geirsdóttir, A, Sigurdsson, H. Metabolic physiology in age related macular degeneration. *Prog Retin Eye Res*. 2011;30(1):72–80.
47. Grimm, D, Streetz, KL, Jopling, CL, Storm, TA, Pandey, K, Davis, CR, Marion, P, Salazar, F, Kay, MA. Fatality in mice due to oversaturation of cellular microRNA/short hairpin RNA pathways. *Nature*. 2006;441(7092):537–541.
48. Babapoor-Farrokhran, S, Qin, Y, Flores-Bellver, M, Niu, Y, Bhutto, IA, Aparicio-Domingo, S, Guo, C, Rodrigues, M, Domashevich, T, Deshpande, M, Megarity, H, Chopde, R, Eberhart, CG, Canto-Soler, V, Montaner, S, Sodhi, A. Pathologic vs. protective roles of hypoxia-inducible factor 1 in RPE and photoreceptors in wet vs. dry age-related macular degeneration. *Proc Natl Acad Sci U S A*. 2023;120(50):e2302845120.
49. Landfried, B, Samardzija, M, Barben, M, Schori, C, Klee, K, Storti, F, Grimm, C. Digoxin-induced retinal degeneration depends on rhodopsin. *Cell Death Dis*. 2017;8(3):e2670.
50. Chen, R, Ahmed, MA, Forsyth, NR. Dimethyloxalylglycine (DMOG), a Hypoxia Mimetic Agent, Does Not Replicate a Rat Pheochromocytoma (PC12) Cell Biological Response to Reduced Oxygen Culture. *Biomolecules*. 2022;12(4)
51. Zhdanov, AV, Okkelman, IA, Collins, FW, Melgar, S, Papkovsky, DB. A novel effect of DMOG on cell metabolism: direct inhibition of mitochondrial function precedes HIF target gene expression. *Biochim Biophys Acta*. 2015;1847(10):1254–1266.
52. Grimm, C, Wenzel, A, Groszer, M, Mayser, H, Seeliger, M, Samardzija, M, Bauer, C, Gassmann, M, Remé, CE. HIF-1-induced erythropoietin in the hypoxic retina protects against light-induced retinal degeneration. *Nat Med*. 2002;8(7):718–724.
53. Le, YZ, Zheng, W, Rao, PC, Zheng, L, Anderson, RE, Esumi, N, Zack, DJ, Zhu, M. Inducible expression of cre recombinase in the retinal pigmented epithelium. *Invest Ophthalmol Vis Sci*. 2008;49(3):1248–1253.
54. Bartoszewski, R, Moszyńska, A, Serocki, M, Cabaj, A, Polten, A, Ochocka, R, Dell'Italia, L, Bartoszewska, S, Króliczewski, J, Dąbrowski, M, Collawn, JF. Primary endothelial cell-specific regulation of hypoxia-inducible factor (HIF)-1 and HIF-2 and their target gene expression profiles during hypoxia. *FASEB J*. 2019;33(7):7929–7941.

55. Chamboredon, S, Ciais, D, Desroches-Castan, A, Savi, P, Bono, F, Feige, JJ, Cherradi, N. Hypoxia-inducible factor-1α mRNA: a new target for destabilization by tristetraprolin in endothelial cells. *Mol Biol Cell*. 2011;22(18):3366–3378.
56. Balakrishnan, B, Jayandharan, GR. Basic biology of adeno-associated virus (AAV) vectors used in gene therapy. *Curr Gene Ther*. 2014;14(2):86–100.
57. Mingozzi, F, High, KA. Immune responses to AAV vectors: overcoming barriers to successful gene therapy. *Blood*. 2013;122(1):23–36.
58. Burnett, JC, Rossi, JJ, Tiemann, K. Current progress of siRNA/shRNA therapeutics in clinical trials. *Biotechnol J*. 2011;6(9):1130–1146.
59. Whitehead, KA, Langer, R, Anderson, DG. Knocking down barriers: advances in siRNA delivery. *Nat Rev Drug Discov*. 2009;8(2):129–138.

Supplementary Figures

Figure S1 | Schematic representation of shRNAmiR constructs with the miR-E backbone and shHif1a, shHif2a and shCtrl target sequences.

(A-C) Sequences of the shRNAmiR constructs. Restriction enzymes used for cloning, the 5' complement, the basal stem, the target sequence, and the 3' flank are indicated.

Figure S2 | Evaluation of shHif2_1-6 in 661W cells

Hif2a mRNA levels in 661W cell lines stably expressing shCtrl or shHif2_1-6. Expression was normalized to beta-actin (*Actb*) and shown relative to expression of shCtrl (set to 1). Shown are means and individual values, n=2.

Figure S3 | Safety assessment of AAV-shHif injection in wt mice

(A) GFP fluorescence and immunostainings in retinal cross-sections of wt mice injected with PBS, shCtrl, or shHif at 3 wpi. Green: GFP; magenta/white: IBA1; grey: DAPI (nuclear stain). Shown are merged images (left) and single-channel images for IBA1 (right). RPE: retinal pigment epithelium. ONL: outer nuclear layer. INL: inner nuclear layer. GCL: ganglion cell layer. **(B)** Representative flatmount images of retina (top) and corresponding RPE (bottom) of wt mice injected with shCtrl (left) or shHif (right) at 3 wpi. GFP and mCherry fluorescence indicate the transduced area. Arrows: injection site. Antibodies for cone arrestin (ARR3, white) and beta-catenin (CTNB1, white) were used to stain cone photoreceptors and RPE cells, respectively. **(C)** Light microscopic images of panorama sections through retinas of wt mice injected with shCtrl (left) or shHif (right) at 22 wpi. Scale bar as indicated.

Figure S4 | Phenotype of *RPE*$^{\Delta Vegfa}$ mice.

Light microscopic panorama image of a retina section from an *RPE*$^{\Delta Vegfa}$ mouse (injected with $1x10^9$ vg/µL AAV::VMD2-Cre-P2A-eGFP) at 39 wpi. The area transduced with the virus resulting in an RPE-specific *Vegfa* knockout is marked. Insets: higher magnifications of

boxed areas. RPE: retinal pigment epithelium. PS: photoreceptor segments. ONL: outer nuclear layer. INL: inner nuclear layer. GCL: ganglion cell layer. Scale bar as indicated.

Supplemental data file 1 | AAV-plasmid sequences for shHif and shCtrl.

The shHif1, shHif2, and shCtrl sequences are highlighted in red, green, and blue, respectively.

Table 1 | Primer sequences for real-time PCR

Gene	Forward primer (5'-3')	Reverse Primer (5'-3')
	Mouse genes	
Actb	CAACGGCTCCGGCATGTGC	CTCTTGCTCTGGGCCTCG
Hif1a	CAATGTCTCCTTTACCTTCATCGG	TGGATTCTTTGCCTCTGTGTCTTC
Hif2a	GGAGCTCAAAAGGTGTCAGG	CAGGTAAGGCTCGAACGATG
Slc2a1	AGTGTATCCTGTTGCCCTTCTG	GCCGACCCTCTTCTTTCATCTC
Casp1	GGCAGGAATTCTGGAGCTTCAA	GTCAGTCCTGGAAATGTGCC
Pde6b	TCTGGAGGATTGCCTGGTG	GGCGAATGAGCTGAAGTGG
Rpe65	AAAGCAGACAAGGAAGATCCAA	CCCAAAGACTCCACGAAGAA
	Human genes	
ACTB	CCTGGCACCCAGCACAAT	GGGCCGGACTCGTCATAC
VEGFA	GTGGACATCTTCCAGGAGTACC	TGTTGTGCTGTAGGAAGCTCAT
ANGPTL4	AGAGGCAGAGTGGACTATTTG	TGGCGCCTCTGAATTACTG
SERPINE1	ACAAATCAGACGGCAGCAC	TAGGGCAGTTCCAGGATGTC
CFH	GTGACACAGATGGATGGAC	CGATCTGGTTCCATTGCAC
GNAT2	CTGCTACTGCTGGGTGCT	TGGTGAATAGCCATCCTGGT

Table 2 | Treatment groups and AAVs

Treatment group	Mouse strain	Capsid	DNA construct
		Single AAV injections	
WT + shCtrl	B6/J-Crl1	AAV8-TM	GRK1-GFP-shCtrl-VMD2-mCherry-shCtrl
WT + shHif	B6/J-Crl1	AAV8-TM	GRK1-GFP-shHif1-VMD2-mCherry-shHif2
Rod$^{\Delta Vhl}$ + shCtrl	*Vhl$^{fl/fl}$;Opsin-Cre*	AAV8-TM	GRK1-GFP-shCtrl-VMD2-mCherry-shCtrl
Rod$^{\Delta Vhl}$ + shHif	*Vhl$^{fl/fl}$;Opsin-Cre*	AAV8-TM	GRK1-GFP-shHif1-VMD2-mCherry-shHif2
Vegfa$^{fl/fl}$ + GFP	*Vegfa$^{fl/fl}$*	AAV4	VMD2-eGFP
RPE$^{\Delta Vegfa}$	*Vegfa$^{fl/fl}$*	AAV4	VMD2-Cre-P2A-eGFP
		Double AAV injections (combined with AAV4/2::VMD2-Cre-P2A-GFP)	
RPE$^{\Delta Vegfa}$ + shCtrl	*Vegfa$^{fl/fl}$*	AAV8-TM	GRK1-GFP-shCtrl-VMD2-mCherry-shCtrl
RPE$^{\Delta Vegfa}$ + shHif	*Vegfa$^{fl/fl}$*	AAV8-TM	GRK1-GFP-shHif1-VMD2-mCherry-shHif2
RPE$^{\Delta Vegfa}$ + shHif1	*Vegfa$^{fl/fl}$*	AAV8-TM	GRK1-GFP-shHif1
RPE$^{\Delta Vegfa}$ + shHif2	*Vegfa$^{fl/fl}$*	AAV8-TM	VMD2-mCherry-shHif2
		PBS and uninjected	
Vhl$^{fl/fl}$	*Vhl$^{fl/fl}$*	n.a.	n.a.
Vegfa$^{fl/fl}$	*Vegfa$^{fl/fl}$*	n.a.	n.a.
Vegfa$^{fl/fl}$ + PBS	*Vegfa$^{fl/fl}$*	n.a.	n.a. (PBS)

All AAVs have type 2 ITRs. AAV8-TM: AAV8-tripple mutation (Y447F + Y733F + T494V)

Table 3 | Primary antibodies used for immunofluorescence and Western blotting

Antibody	Cat. Number	Research Resource Identifier (RRID)	Vendor	Application	Dilution
IBA1	019-19741	AB_839504	Wako Pure Chemical Industries	Immunofluorescence	1:500
ARR3	AB15282	AB_1163387	Merck KGaA	Immunofluorescence	1:1000
PODXL	AF1556	AB_354858	R&D Systems	Immunofluorescence	1:200
CTNB1	610153	AB_397554	BD Transduction Laboratories™	Immunofluorescence	1:500
Cre	69050-3	AB_10806983	Merck	Immunofluorescence	1:300
HIF2A	AB199	AB_302739	Abcam	Western blotting	1:500
HIF1A	NB100-479	AB_10000633	Novus Biologicals	Western blotting	1:2000
ACTB	A5441	AB_476744	Sigma	Western blotting	1:10000

Figure 1

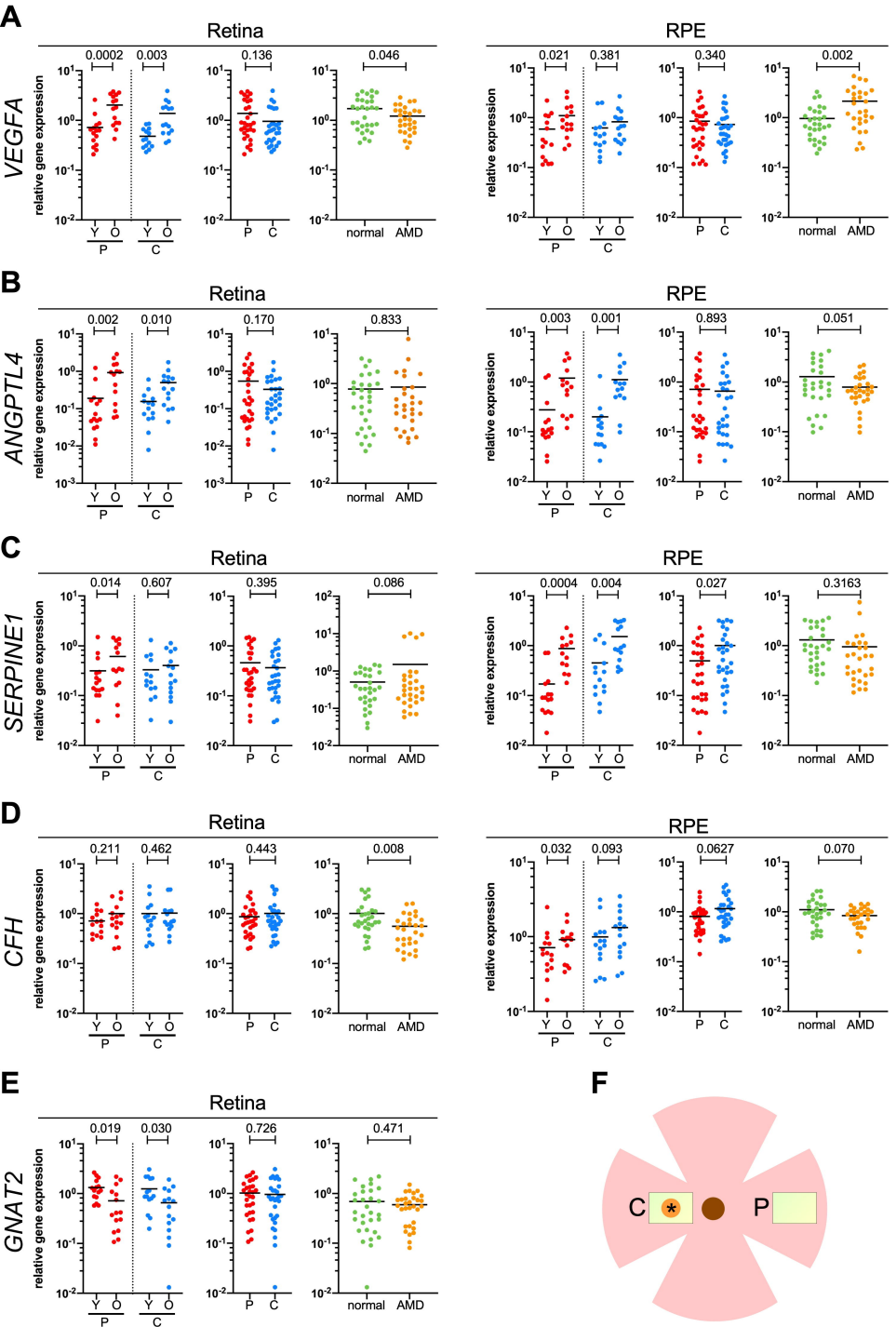
A
Retina
RPE
VEGFA
relative gene expression
relative expression
0.0002
0.003
0.136
0.046
0.021
0.381
0.340
0.002
B
ANGPTL4
0.002
0.010
0.170
0.833
0.003
0.001
0.893
0.051
C
SERPINE1
0.014
0.607
0.395
0.086
0.0004
0.004
0.027
0.3163
D
CFH
0.211
0.462
0.443
0.008
0.032
0.093
0.0627
0.070
E
GNAT2
0.019
0.030
0.726
0.471
Y O
P
C
normal
AMD
F
C
P

Figure 2

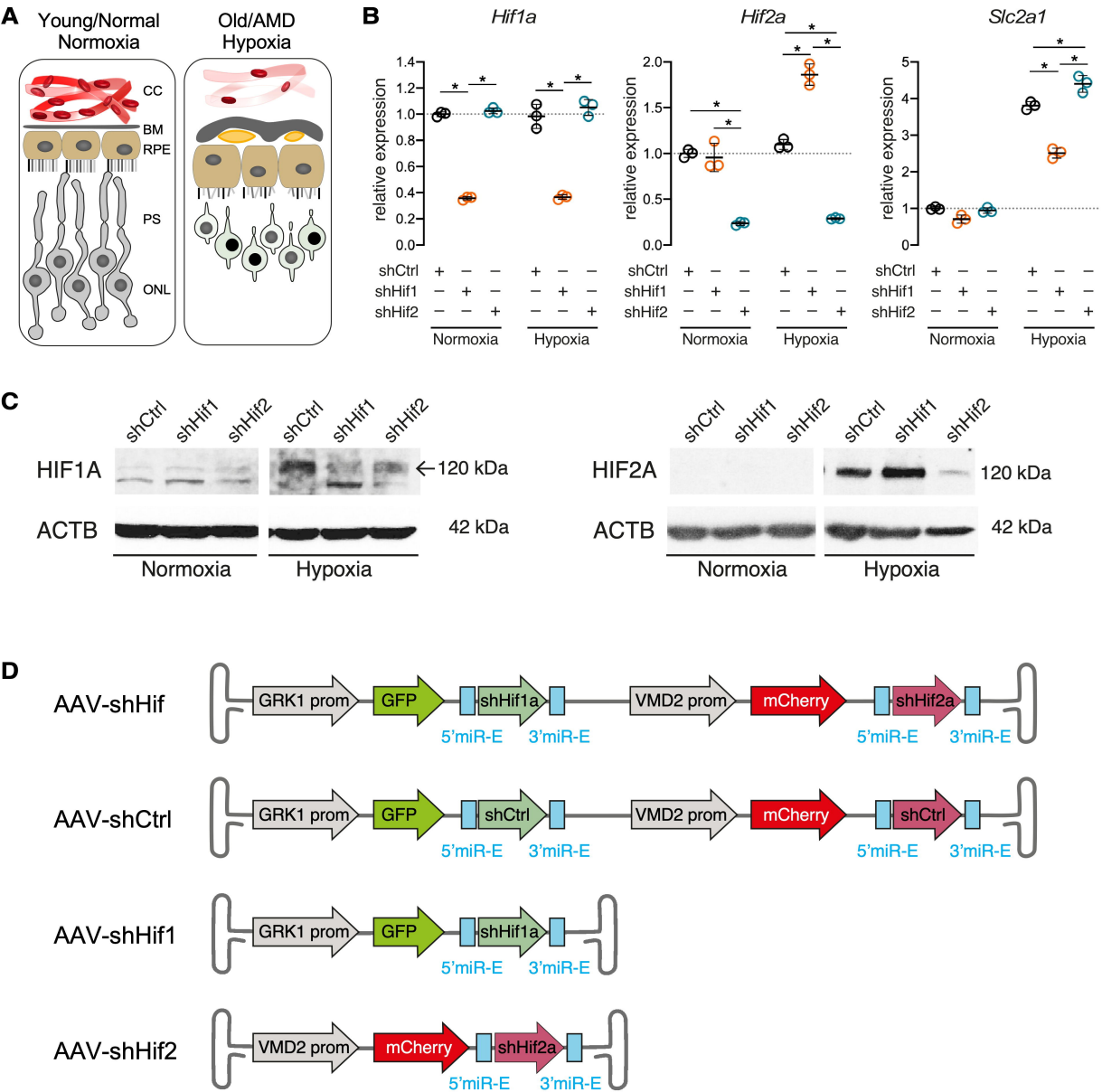
A
Young/Normal
Normoxia
Old/AMD
Hypoxia
CC
BM
RPE
PS
ONL
B
Hif1a
Hif2a
Slc2a1
relative expression
shCtrl
shHif1
shHif2
Normoxia
Hypoxia
C
HIF1A
ACTB
120 kDa
42 kDa
HIF2A
D
AAV-shHif
AAV-shCtrl
AAV-shHif1
AAV-shHif2
GRK1 prom
GFP
shHif1a
VMD2 prom
mCherry
shHif2a
shCtrl
5'miR-E
3'miR-E

Figure 3

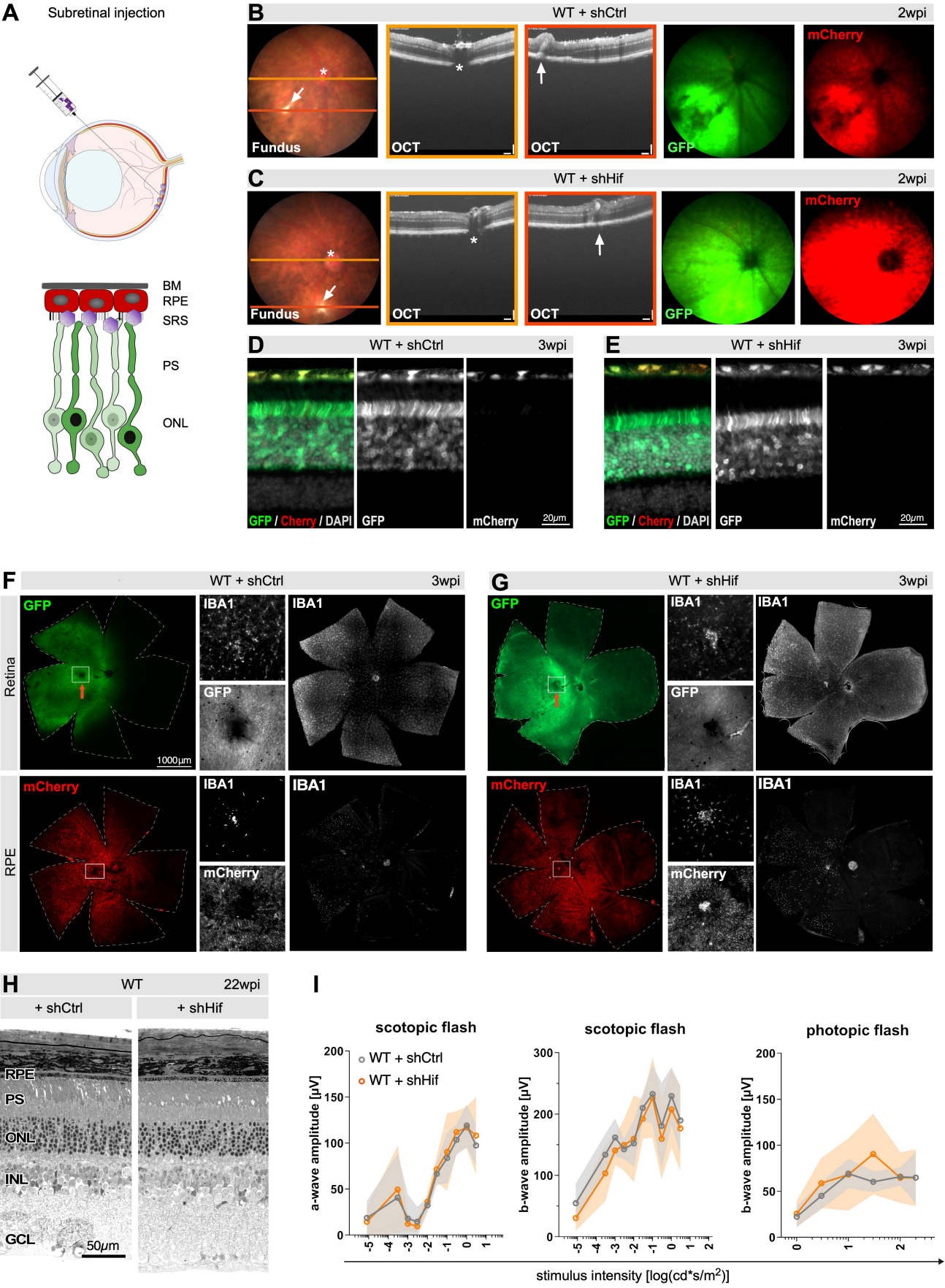
A
Subretinal injection
BM
RPE
SRS
PS
ONL
B
WT + shCtrl
2wpi
Fundus
OCT
OCT
GFP
mCherry
C
WT + shHif
2wpi
Fundus
OCT
OCT
GFP
mCherry
D
WT + shCtrl
3wpi
GFP / Cherry / DAPI
GFP
mCherry
20µm
E
WT + shHif
3wpi
GFP / Cherry / DAPI
GFP
mCherry
20µm
F
WT + shCtrl
3wpi
Retina
GFP
IBA1
IBA1
GFP
1000µm
RPE
mCherry
IBA1
IBA1
mCherry
G
WT + shHif
3wpi
GFP
IBA1
IBA1
GFP
mCherry
IBA1
IBA1
mCherry
H
WT
22wpi
+ shCtrl
+ shHif
RPE
PS
ONL
INL
GCL
50µm
I
scotopic flash
scotopic flash
photopic flash
WT + shCtrl
WT + shHif
a-wave amplitude [µV]
b-wave amplitude [µV]
b-wave amplitude [µV]
stimulus intensity [log(cd*s/m2)]

Figure 4

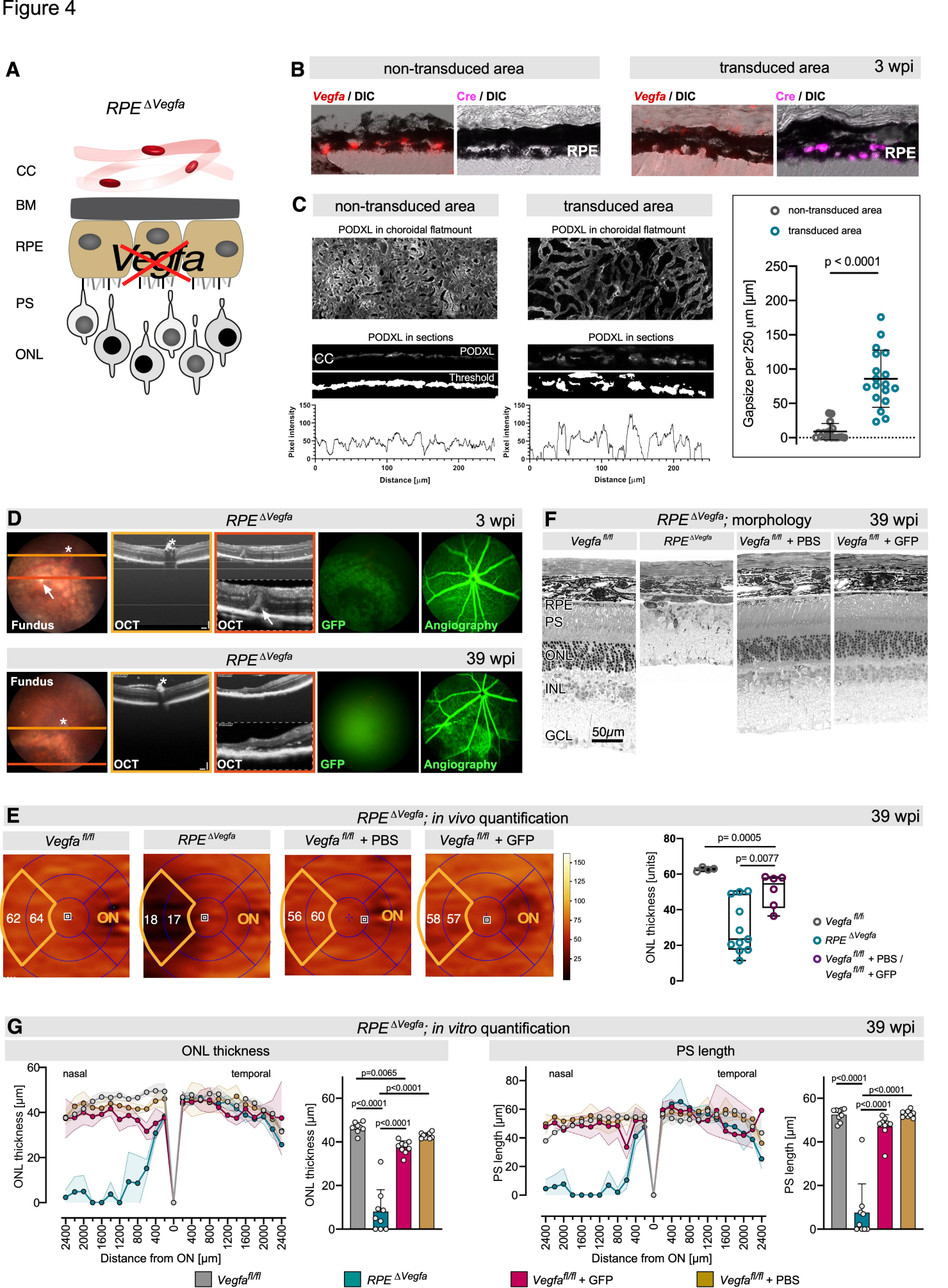
A
RPE ΔVegfa
CC
BM
RPE
PS
ONL
Vegfa
B
non-transduced area
transduced area
3 wpi
Vegfa / DIC
Cre / DIC
RPE
C
non-transduced area
transduced area
PODXL in choroidal flatmount
PODXL in sections
CC
PODXL
Threshold
Pixel intensity
Distance [µm]
non-transduced area
transduced area
p < 0.0001
Gapsize per 250 µm [µm]
D
RPE ΔVegfa
3 wpi
39 wpi
Fundus
OCT
GFP
Angiography
F
RPE ΔVegfa; morphology
39 wpi
Vegfa fl/fl
RPE ΔVegfa
Vegfa fl/fl + PBS
Vegfa fl/fl + GFP
RPE
PS
ONL
INL
GCL
50µm
E
RPE ΔVegfa; in vivo quantification
39 wpi
Vegfa fl/fl
RPE ΔVegfa
Vegfa fl/fl + PBS
Vegfa fl/fl + GFP
62 64
18 17
56 60
58 57
ON
ONL thickness [units]
p= 0.0005
p= 0.0077
Vegfa fl/fl
RPE ΔVegfa
Vegfa fl/fl + PBS /
Vegfa fl/fl + GFP
G
RPE ΔVegfa; in vitro quantification
39 wpi
ONL thickness
PS length
nasal
temporal
ONL thickness [µm]
PS length [µm]
Distance from ON [µm]
p=0.0065
p<0.0001
Vegfa fl/fl
RPE ΔVegfa
Vegfa fl/fl + GFP
Vegfa fl/fl + PBS

Figure 5

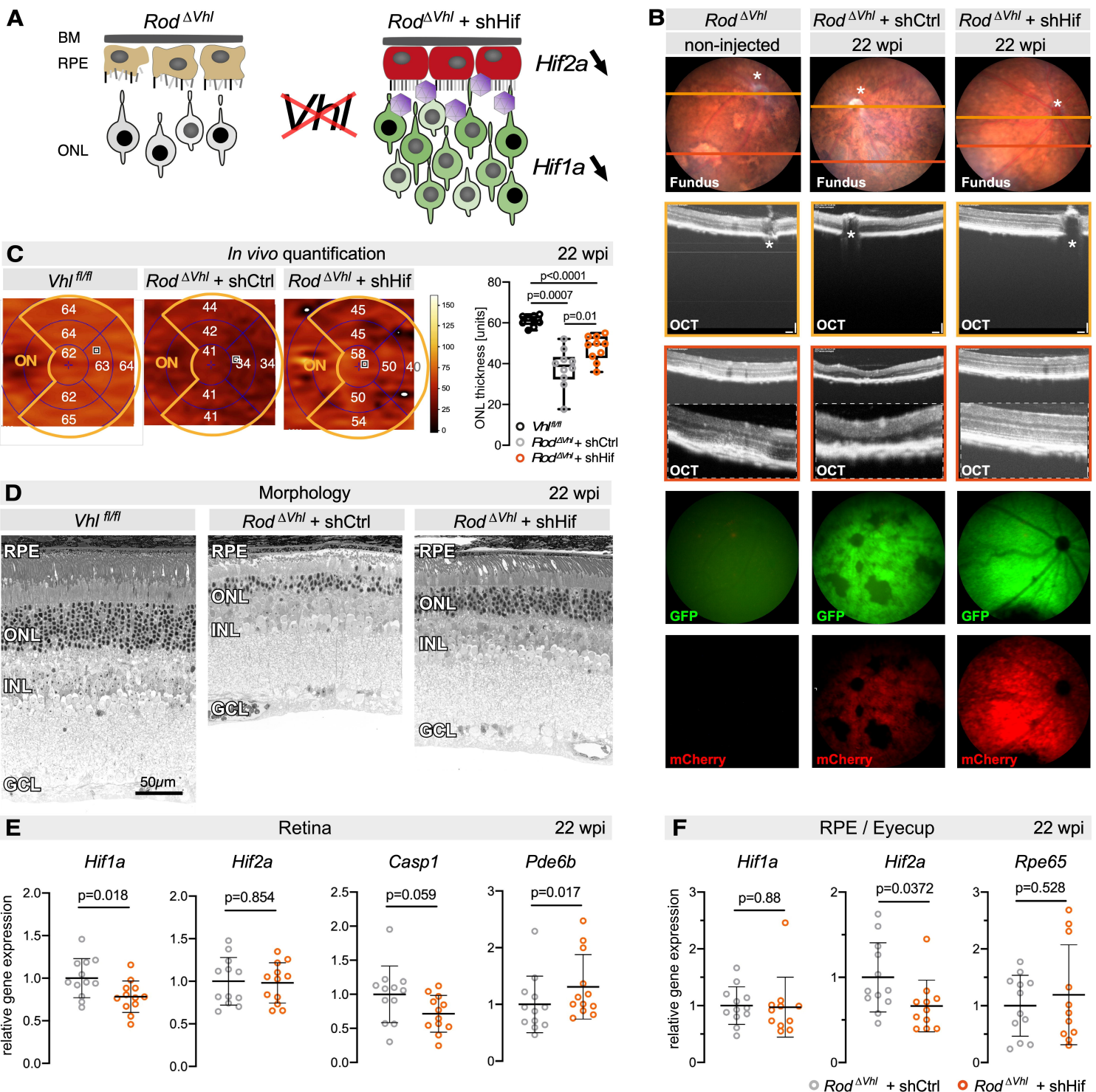
A
Rod ΔVhl
BM
RPE
ONL
Vhl
Rod ΔVhl + shHif
Hif2a
Hif1a
B
Rod ΔVhl
non-injected
Rod ΔVhl + shCtrl
22 wpi
Rod ΔVhl + shHif
22 wpi
Fundus
OCT
GFP
mCherry
C
In vivo quantification
22 wpi
Vhl fl/fl
Rod ΔVhl + shCtrl
Rod ΔVhl + shHif
ON
ONL thickness [units]
p<0.0001
p=0.0007
p=0.01
Vhl fl/fl
Rod ΔVhl + shCtrl
Rod ΔVhl + shHif
D
Morphology
22 wpi
Vhl fl/fl
Rod ΔVhl + shCtrl
Rod ΔVhl + shHif
RPE
ONL
INL
GCL
50µm
E
Retina
22 wpi
Hif1a
Hif2a
Casp1
Pde6b
relative gene expression
p=0.018
p=0.854
p=0.059
p=0.017
F
RPE / Eyecup
22 wpi
Hif1a
Hif2a
Rpe65
relative gene expression
p=0.88
p=0.0372
p=0.528
Rod ΔVhl + shCtrl
Rod ΔVhl + shHif

Figure 6

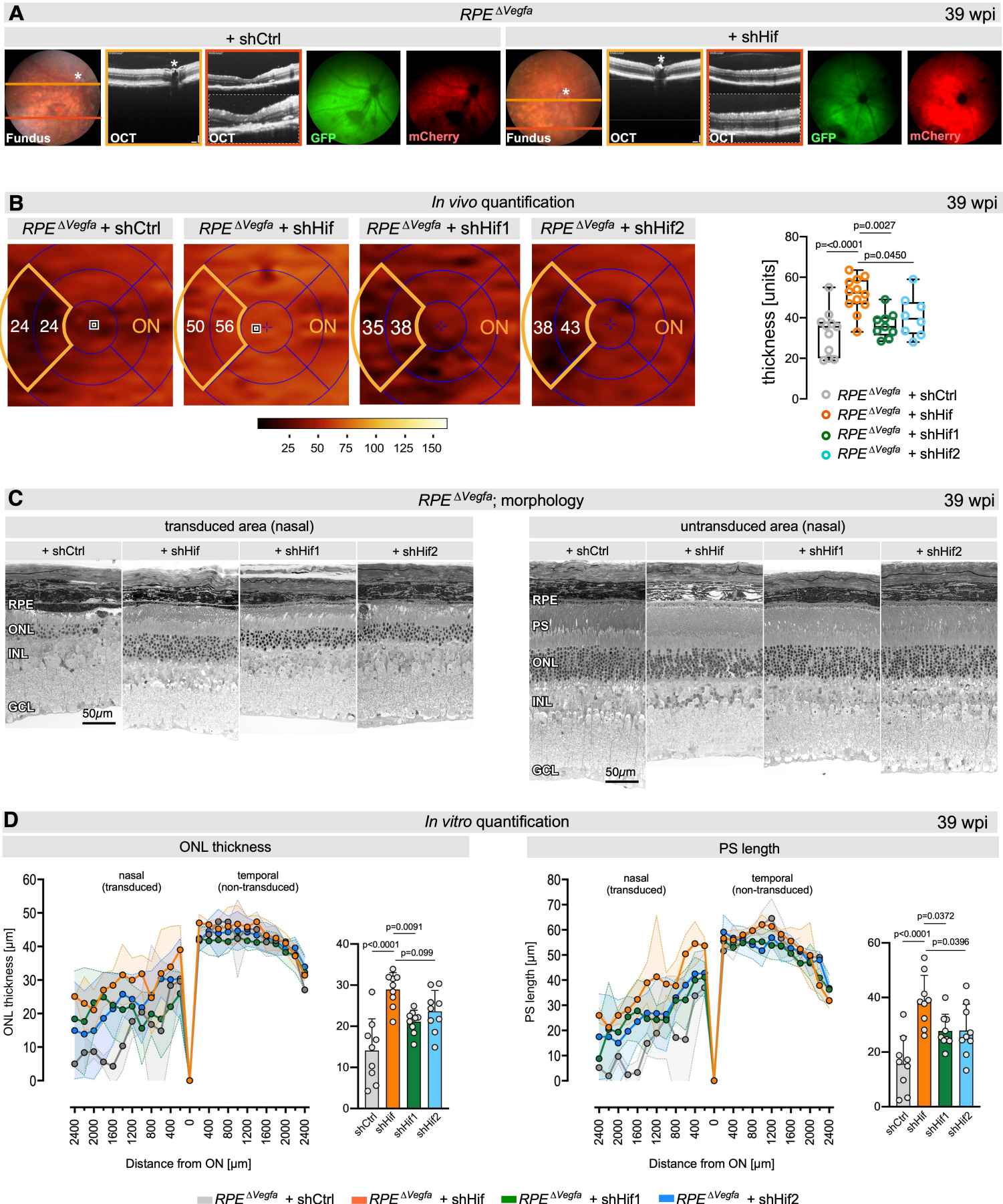
A
RPE ΔVegfa
39 wpi
+ shCtrl
+ shHif
Fundus
OCT
OCT
GFP
mCherry
Fundus
OCT
OCT
GFP
mCherry
B
In vivo quantification
39 wpi
RPE ΔVegfa + shCtrl
RPE ΔVegfa + shHif
RPE ΔVegfa + shHif1
RPE ΔVegfa + shHif2
24 24 ON
50 56 ON
35 38 ON
38 43 ON
25 50 75 100 125 150
thickness [units]
p=0.0027
p=<0.0001
p=0.0450
RPE ΔVegfa + shCtrl
RPE ΔVegfa + shHif
RPE ΔVegfa + shHif1
RPE ΔVegfa + shHif2
C
RPE ΔVegfa; morphology
39 wpi
transduced area (nasal)
+ shCtrl
+ shHif
+ shHif1
+ shHif2
RPE
ONL
INL
GCL
50µm
untransduced area (nasal)
+ shCtrl
+ shHif
+ shHif1
+ shHif2
RPE
PS
ONL
INL
GCL
50µm
D
In vitro quantification
39 wpi
ONL thickness
nasal (transduced)
temporal (non-transduced)
ONL thickness [µm]
Distance from ON [µm]
p=0.0091
p<0.0001
p=0.099
shCtrl
shHif
shHif1
shHif2
PS length
nasal (transduced)
temporal (non-transduced)
PS length [µm]
Distance from ON [µm]
p=0.0372
p<0.0001
p=0.0396
shCtrl
shHif
shHif1
shHif2
RPE ΔVegfa + shCtrl
RPE ΔVegfa + shHif
RPE ΔVegfa + shHif1
RPE ΔVegfa + shHif2

Figure 7

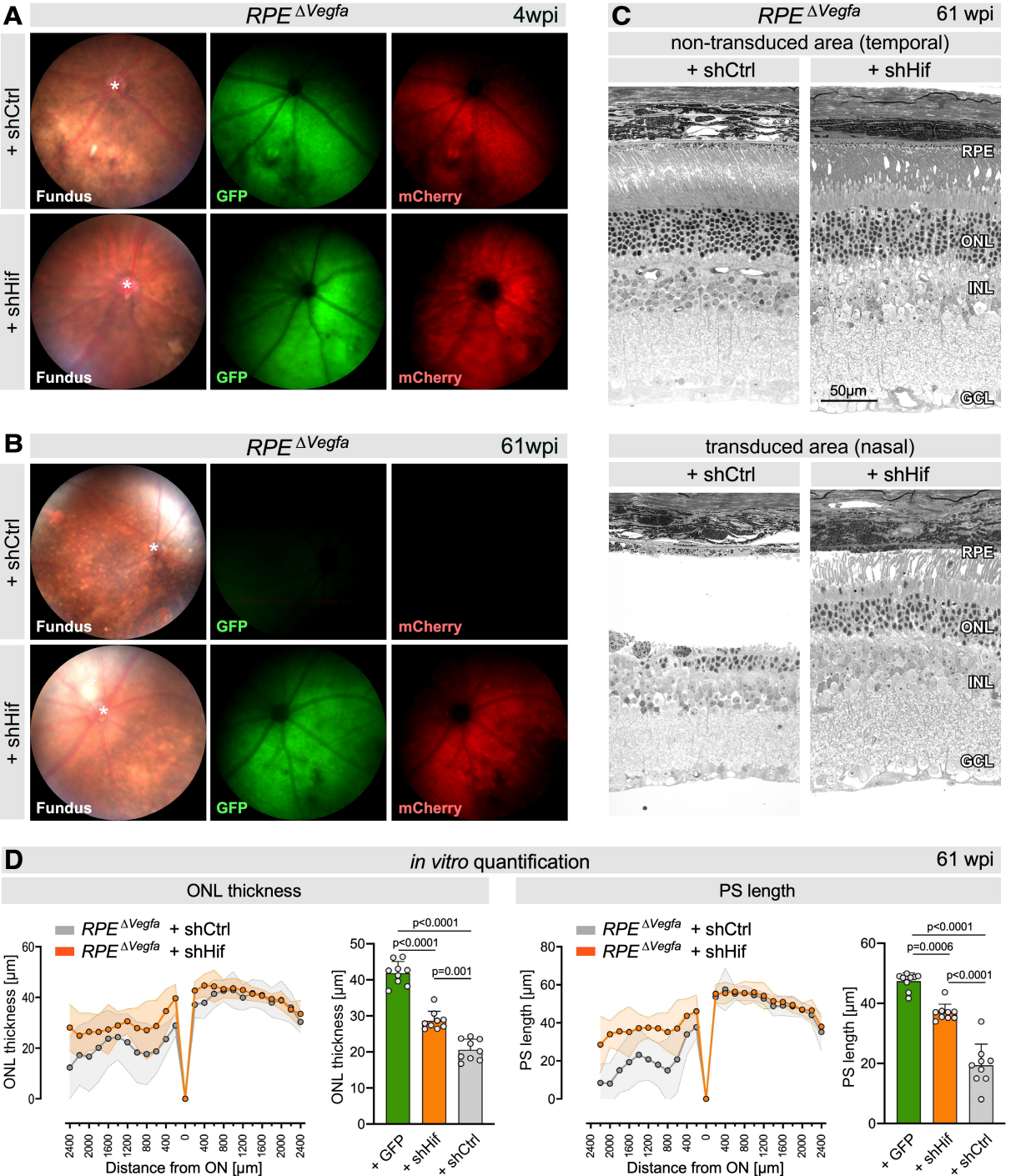
A
RPE ΔVegfa
4wpi
+ shCtrl
+ shHif
Fundus
GFP
mCherry
B
RPE ΔVegfa
61wpi
C
RPE ΔVegfa
61 wpi
non-transduced area (temporal)
transduced area (nasal)
+ shCtrl
+ shHif
RPE
ONL
INL
GCL
50µm
D
in vitro quantification
61 wpi
ONL thickness
PS length
ONL thickness [µm]
PS length [µm]
Distance from ON [µm]
p<0.0001
p=0.001
p=0.0006
+ GFP
+ shHif
+ shCtrl